Zinc-rich clays in supergene non-sulfide zinc deposits

Flavien Choulet, M. Buatier, Luc Barbanson, Régis Guégan, A. Ennaciri

▶ **To cite this version:**

HAL Id: insu-01239887

https://insu.hal.science/insu-01239887

Submitted on 10 Dec 2015

Zinc-rich clays in supergene non-sulfide deposits.

1   **"Fertilization" of barren clays in supergene non-sulphide zinc deposits**

2

3   Choulet F.[1, *], Buatier M.[2], Barbanson L.[2], Guégan R.[2], Ennaciri A.[3]

4

5   *[1]: Chrono-Environnement, Université de Franche-Comté/CNRS (UMR6249), Besançon, France*

6   *[2]: ISTO, Université d'Orléans/CNRS (UMR7327), Orléans, France*

7   *[3]: Groupe Managem, Casablanca, Morocco*

8   *[*]:* **corresponding author** flavien.choulet@univ-fcomte.fr

9

10   **Abstract**

11

12   The nature and the origin of zinc clays are poorly understood. Based on the example of the

13   Bou Arhous Zn-Pb ore deposit in the Moroccan High Atlas, this study presents new advances for the

14   characterization of barren and mineralised clays associated to zinc non-sulphide ores. In the field, white

15   to ochre granular clays are associated with willemite, whilst red smooth clays fill karst-related cavities

16   cutting across the non-sulphide ore bodies. Red clays (kaolinite chlorite, illite and smectite) present

17   evidence of stratification that reflects internal sedimentation processes during karst evolution. White

18   clays contain 7Å-clay mineral/smectite irregular mixed layers with less than 20% of smectite layers.

19   The willemite crystals are partially dissolved and are surrounded by authigenic zinc clay minerals.

20   WDS analyses on newly formed clay aggregates have revealed that this mixed layered mineral is

21   composed by fraipontite and sauconite. CEC measurements support that zinc is only located within the

22   octahedral sheets. These new results support the following process: 1) dissolution of willemite, leading

23   to releasing Si and Zn, 2) interaction between Zn-Si rich solutions and residual-detrital clays, 3)

24   neogenesis of mixed-layered zinc clay minerals that grow over detrital micas, representing the source

25   for Al.

26

27   **Keyword:** supergene zinc deposits, karst, clay minerals, Morocco

28

29   **1) Introduction**

30

Clays are often considered to be a knotty challenge for ore processing (**Connelly 2011**; **Lim 2011**), because of their size and shape characteristics. The typical problems met by the mining industry encompass the difficulties of handling, crushing, screening, milling and classifying clay-rich raw material. High grade of clay results in poor selectivity and thus significantly slow flotation kinetics (e.g. **Bayraktar et al. 1998**; **Fuerstenau et al. 2007**). Occurrence of clays in the ore may also affect leaching techniques by increasing pulp viscosity. Despite many efforts to fathom these crucial difficulties, cost of solutions is considerable and hence clays act as a brake on ore extraction and processing. Another difficulty with clays associated to ores is their potential to trap metal (**Newman 1987**). Hence a noteworthy amount of economic elements is captured in clays, which are often difficult to process for recovery (e.g. Ni-rich clays, **Crundwell et al. 2011**). Understanding the nature and the origin of clays associated to ores is critical for designing flowsheet and identifying potential unconventional sources for critical metal extraction and recovery.

Recent development of coupled techniques of leaching, solvent extraction and electrowinning and their application to zinc smelting (**Gnoinski 2006; de Wet and Singleton 2008; Abkhoshk et al. 2014**) have contributed to revive interest in the disregarded non-sulphide deposits with successful application in Namibia, Peru and Morocco. Supergene non-sulphide zinc deposits are formed during weathering in relation with tectonics and climate (**Hitzman et al. 2003**). Such deposits are described around the world and occur in various geological environments, from silicoclastic to carbonate host rocks (**Boni and Large 2003**). Based on genetic processes at their origin, three types of supergene deposits have been distinguished: 1) direct-replacement deposits, 2) wall-rock deposits and 3) karst-filling deposits (**Hitzman et al. 2003**). These different processes may occur together in a given deposit, affecting the texture of ores and providing an intricate mineralogical record. This includes carbonates (smithsonite), hydrated carbonates (hydrozincite), silicates (willemite), hydrated silicates (hemimorphite) and various rare minerals, including clays such as sauconite, a smectite containing up to 50 %wt of ZnO (**Ross 1946**) or more rarely fraipontite, a zinc bertherine (**Fransolet and Bourguignon 1975**).

In many supergene zinc deposits, mineralised clay material represents a significant economic resource that cannot be ignored (e.g. up to 30 % of the ore at Accha in Peru, **Boni et al. 2009a**). The occurrence of such amount of clays in the ore requires desliming and results in lower zinc recovery (**de Wet and Singleton 2008**), although the impact of clays is probably lower than expected from

61 mineralurgical tests (**Boni et al. 2009b**). Besides, the ability of clays to sorb or catch Zn^{2+} cations

62 located within the interlayer space of swelling clays is well known (**Bradbury and Baeyens 1999**;

63 **Churakov and Dähn 2012**), implying natural clays may represent an economic potential of zinc

64 recovery without much efforts. Although zinc enriched clays are frequently described in supergene

65 deposits, clear identification of the nature of clay minerals remains rare and the classical sauconite

66 assessment is highly speculative. In addition, the origin of zinc clays and its place within the ore

67 evolution remain badly understood.

68 This study investigates the characterisation of zinc clays of the Bou Arhous deposit in the

69 Moroccan High Atlas. This deposit is hosted in Lower Jurassic limestone, and ore is mainly willemite,

70 whose origin is not clearly understood (**Choulet et al. 2014**). Willemite is associated to various types

71 of clayey material, presenting differences in mineralogy, texture and Zn content. The Bou Arhous ore

72 deposit represents a key natural example to understand the origin of zinc-bearing clays and their place

73 in the ore deposition. Using microscopic observations and classical techniques for investigating clay

74 minerals, we aim at characterizing the nature of clays recorded at Bou Arhous and debate on their

75 origin. Further quantification of the cation exchange capacity (CEC) allows us to discuss the potential

76 of zinc recovery.

77

78 **2) Geological setting of the Bou Arhous ore deposit**

79

80 The Bou Arhous Pb-Zn ore deposit (32.27°N, 3.76°W) is located in the Moroccan High Atlas

81 range, 60 km to the north-east of Errachidia city (**Fig. 1A**). The local geology of this deposit has been

82 extensively studied by Leblanc (**1968**) and recently revisited in Choulet et al. (**2014**).

83 The formation of the High Atlas intra-continental fold-and-thrust belt (**Mattauer et al. 1977**)

84 results from the far-field effect of the Alpine collision events since mid-Tertiary (ca. 40 Ma) and up to

85 Pleistocene (**Frizon de Lamotte et al. 2009**). As a consequence, the Mesozoic sedimentary basins

86 formed during the opening of Tethys and Atlantic Oceans have been affected by inversion tectonics

87 accompanied by regional uplift and localized exhumation of Lower Jurassic and Triassic strata in the

88 core of narrow anticlines. Thereafter, exhumed strata experienced surface weathering leading to the

89 karst development in the Jurassic limestone (**Choulet et al. 2014; Charles et al. submitted**).

90   The Jbel Bou Arhous range is one of these ENE-WSW trending faulted anticlines that exhume

91   the Triassic and Lower Jurassic strata (**Fig. 1B**). The fold-related "Grand Accident" thrust is rooted in

92   the Triassic substratum (**Figs. 1B and 1C**; **Teixell et al. 2003**) and represents a reactivated normal fault

93   that delimitated contrasting paleogeographic domains of the former Tethys Sea (**Warme 1998**). To the

94   north of the fault, deep-seated dolomitic limestone is almost barren, whereas massive limestone of the

95   southern domain originally deposited in reef or para-reef environments includes lenses of base metal

96   sulphides (**Figs. 1B and 1C**). At site of the Bou-Arhous mine located in the footwall of the "Grand

97   Accident" thrust, the two limbs of the anticline are vertical (**Fig. 2A**) or slightly recumbent and the fold

98   hinge is missing (**Fig. 1C**). Host rocks of mineralisation include Sinemurian black limestone, locally

99   interbedded with thin layers of greyish marls (**Fig. 2B**), which have experienced slight dolomitisation

100   during diagenesis and emplacement of base metals sulphide lenses (**Leblanc 1968**). In depth,

101   mineralisation is tectonically juxtaposed along the "Grand Accident" thrust to the Triassic variegated

102   shales associated to gypsum (**Fig. 2C**).

103   Following exploration campaigns in the 1960's, the Bou Arhous mine has been exploited by

104   Managem since the early 2000's and reserves have been estimated at 250 kt grading 4 % Pb and 16 %

105   Zn. Mineralisation consists of an intricate network of various-sized veins, extending over 18000 square

106   metres. Veins up to 10 metres in width parallel the stratification and dip steeply to the north (**Fig. 2A**).

107   Non-sulphide zinc-bearing minerals include willemite, hydrozincite, hemimorphite and smithsonite.

108   Gangue minerals include automorphous white carbonates, such as calcite and dolomite (**Fig. 2D**),

109   emplaced during the early sulphide stage (**Choulet et al. 2014**). Willemite is finely associated to galena

110   remnant and cerussite, forming a well-defined black ore. Black ore generally occurs as disseminated

111   patches enclosed in very fine-grained clay-rich material (**Fig. 2E**), showing a variety of colours. Hence,

112   different types of clayey material have been distinguished and they are detailed in the following

113   section.

114

115   **3) The different types of clay deposits at Bou Arhous**

116

117   Previous investigation of the clayey material associated to the mineralisation (**Leblanc 1968**)

118   suggested the existence of two types of clays. Reddish and smooth clays occur as infilling material of

119   the karstic cavities and were considered of detrital origin as evidenced by the layering structures. These

120 clays are barren, but they locally contain some fragments of the non-sulphide mineralisation. In

121 contrast, white and granular clays are frequently associated to willemite and Leblanc (**1968**) suggested

122 that these clays might correspond to newly formed clay minerals with up to 23 % of Zn (**Gaudefroy**

123 **1953**).

124 Based on a recent detailed field study, a new examination of the clay materials has been

125 carried out and we now distinguish three types of clayey material, which may coexist in a same area

126 (**Fig. 3A**).

127 1) Red clayey material fills a network of connected cavities, sinkholes and tunnels, related to the karst

128 of Bou Arhous (**Fig. 3B**). A sub-horizontal bedding (**Fig. 3C**) with evidence of grain size sorting is

129 frequently observed, as well as various-sized clastic fragments of ore and host limestone. The aspect of

130 the red clayey material may be locally smooth, but is often silty or sandy due to millimetre-sized quartz

131 grains. This red clayey material corresponds to the reddish and smooth clays described by Leblanc

132 (**1968**).

133 2) White clayey material occurs as a fine-grained matrix embedding disseminated patches of willemite

134 associated with carbonates and galena. It forms either a thin and partial rim between the black ore and

135 the red clays (**Fig. 3D**), or a widespread impregnation in the mineralisation (**Fig. 3E**). The white colour

136 is not systematic and tends be locally yellowish, indicating a progressive transition to ochre clays. This

137 type partly encompasses the white granular type observed by Leblanc (**1968**).

138 3) A third type, namely ochre clays has been found as cavity-infilling material (**Fig. 3F**) or as a mixture

139 of white and red clayey materials (**Fig. 3A**). Ochre clays share similar features with white clays, such

140 as their association with black ore but this latter one is less preserved than in the case of white clays.

141 Ochre clays may also occur as isolated material without any spatial connection with white and red

142 clays.

143

144 **4) Sampling and methodology**

145

146 *4.1) Bulk chemical composition*

147

148 Fifty-eight rock samples have been collected at Bou Arhous mine and include host-rocks

149 (Triassic shale and Jurassic limestone and marl) and the three types of clayey material (red clays, white

150   clays and ochre clays), listed in **Table 1**. Among them, thirty-four samples have been duplicated for

151   analysing the chemical composition. The chemical composition measurements using acid digestion

152   procedure have been carried out in Managem Group lab, at Marrakech, Morocco. For major elements,

153   0.5 g of a crushed sample (< 200 μm) has been dried and dissolved by fusion at 500°C during 45

154   minutes with 2.5 g of sodium peroxide in a zirconium crucible. The residue was then dissolved in HCl

155   and the solution has been analysed by ICP-AES ULTIMA 2C. For minor elements, a 0.25 g split has

156   been heated (220 °C during 45 minutes) in HCl (50%) – HNO_3 (50%) to fuming and the solution was

157   analysed by ICP-MS Thermo X'Serie 2.

158

159   *4.2) Clay fraction study*

160

161   In addition, for twenty-two samples, the clay fraction (<2 μm) has been separated by

162   decantation using the following procedure. A rock sample has been crushed using a Retsch PM200 ball

163   mill and manually ground in agate mortar. The rock powder has been dissolved in distilled water and

164   dispersed with a magnetic stirrer. Progressive addition of HCl (0.2M) monitored by continuous pH

165   measurements was used to remove carbonate at room temperature. Then, the solution has been washed

166   several times, dispersed and placed in a jar for decantation. After about 4 hours, the first five

167   centimetres of the solution containing the clay suspension (<2 μm) have been withdrawn using a

168   syringe. After removing the supernatant by centrifugation, the residue has been dried and used for

169   further X-ray diffraction (XRD) and cation-exchange capacity measurements.

170   XRD patterns of the whole rock samples and clay fractions have been obtained using a D8

171   Advance Brucker diffractometer equipped with a LinxEye detector, hosted at Utinam lab, Besancon,

172   France. Parallel beam geometry and CuKα radiation at 1.54184 Å has been used. For whole rock

173   sample, the powder was placed in the specimen holder. Acquisition conditions (divergent slit) included

174   a step-scan of 0.5 ° in the 2-52 ° interval, with a step time of 0.05 s. For the clay fraction, the powder

175   has been diluted in distilled water and a drop of the solution has been deposited on a glass lamella for

176   dewatering under air-dried conditions. The orientated-aggregate mount (along c axis) was then placed

177   in holder and a step-scan of 0.02 ° in the 2-30 ° interval, with a step time of 0.5 s has been used for

178   XRD measurements. A duplicate of the orientated-aggregate mount has been treated for ethylene

179   glycol (EG) saturation, by placing the lamella in a pressurised desiccator overnight. For several

samples, a second duplicate has been heated at 550 °C during one hour in a furnace before XRD measurements. EVA software package has been used for data processing and phase identification. The position of 060 reflexion has been determined on clay fraction powders at Institut des Sciences de la Terre d'Orléans, Orléans, France, using an ARL X'TRA diffractometer equipped with Cu anode and a Si solid detector operating at 40 kV and 40 mA. Experimental measurements were carried out at room temperature, with 10 s counting time per 0.02 ° step.

Cation-exchange capacity (CEC) measurements have been carried out at the Institut des Sciences de la Terre d'Orléans, Orléans, France following the procedures described in Meier and Kahr (**1999**) and Ammann et al. (**2005**). A solution of 0.01M Cu(II)-trien sulphate has been prepared from 1.596 g of copper sulphate and 1.508 g of triethylenetetramine. 100+/- 25 mg of clay sample were added to 25 mL of distilled water and to 8 mL of Cu(II)-trien sulphate. The solution has been dispersed using tube roller overnight and was further centrifuged (10 minutes at 6000 rpm) to removed 3 mL of the supernatant. Measurement of $[Cu^{2+}]$ was performed using Atomic Absorption Spectroscopy (AAS) with 2-8100 Polarized Zeeman Hitachi instrumentation and colorimetric techniques. The CEC was then calculated with reference to the dry clay weight, to the water content and to the amount of captured Cu^{2+} ions deduced from AAS measurements. A similar procedure is used for calculating the Zn content in the CEC. Standardisation curves of absorbance for $[Cu^{2+}]$ and $[Zn^{2+}]$ gave coefficients of determination of 0.999 and 0.987, respectively.

4.3) Textural and mineralogical observations

Textural and mineralogical observations have been carried out using optical microscopy (OM) and FEI Quanta 450 Scanning Electron Microscope (SEM) hosted at Femto-ST lab, Besançon, France. The images have been acquired in low vacuum mode (0.7-0.8 mbar) on polished thin sections, with acceleration voltage at 15 kV. An Energy-Dispersive X-Ray Spectrometer (EDS) was coupled to the SEM system providing qualitative determination of the mineral composition using Edax Genesis software package.

4.4) Chemical composition of clay minerals

We have performed quantitative analyses using Cameca SX100 electron microprobe (EPMA), equipped with five Wave-Dispersive X-Ray Spectrometers (WDS) and hosted at Géosciences Montpellier, Montpellier, France. On carbon-coated polished thin-section, we have operated at 20 kV with a beam current at 10 nA. The spot resolution was few micrometres. Quantification of the Na content was not possible due to the interference of the Zn Lβ1 emission line that fall close to the Na Kα emission line.

4) Results

4.1) Whole rock geochemical and mineralogical composition

4.1.1) Host rocks

The Triassic shales are composed of a mixture of quartz, clay minerals, hematite, goethite, and carbonates including both calcite and dolomite (**Table 1**). Gypsum is also present in some samples. The major elements content strongly varies due to a variable proportion of carbonates and iron oxi-hydroxides. Variable enrichment in Zn, Pb, Cu and As can be noticed suggesting the local occurrence of sphalerite, galena, and/or other minor metal-bearing minerals.

Jurassic rocks including marl and limestone contain clay minerals, calcite, dolomite and quartz (**Table 1**). Goethite is common. The SiO_2 and CaO contents are variable and probably mirror the variable abundance in quartz and carbonate in the samples. Minor elements (Zn, Pb, Cu and As) content remains low except for one sample that contains galena, sphalerite and their respective alteration products.

4.1.2) Clayey material

The mineralogy of the red clayey material is characterized by a mixture of quartz, clay minerals, calcite with goethite and rare dolomite (**Table 1**). Despite important variations of CaO and SiO_2 related to carbonate enrichment of some samples (e.g. BA101), the major elements content remains constant. The red clay samples do not display any significant variations of the minor elements content except for Pb and Zn, which display highly variable amounts (e.g. between 830 ppm and 47300

8

239 ppm for Zn); this could be related to the occurrence of willemite and cerussite impurities in these

240 samples.

241   The white clayey material is composed of a mixture of willemite, galena, quartz, clay minerals

242 and carbonate (dolomite, calcite, and cerussite). Dolomite is almost always observed in white clays,

243 marking a noteworthy difference with red clayey material. The MgO content can therefore reach up to

244 10 %wt (**Table 1**). The occurrence of Zn and Pb ore in white clays is responsible for high Zn and Pb

245 grade (up to 320000 ppm for Zn and 37100 ppm for Pb).

246   In ochre clayey material, clay minerals, quartz, calcite and dolomite are always present, with a

247 common occurrence of cerussite. Chemical compositions of the ochre and white clayey materials are

248 relatively close; indeed they have similar MgO and CaO contents (**Table 1**). Despite the absence of Zn-

249 bearing phases (sulphide or carbonate) detected from whole-rock XRD analysis, the Zn content varies

250 between 6275 ppm and 237000 ppm.

251

252   The extreme variations of the Zn content in the three types of clayey material cannot be

253 correlated straightforwardly to the mineralogical composition deduced from whole rock XRD

254 measurement, it may be partly due to the presence of willemite impurities, but, for several samples

255 (ochre clays), Zn-bearing clays must be involved to explain tremendous Zn contents, requiring a

256 specific study of the clay fraction.

257

258 *4.2) Mineralogical characterisation of the clay fraction*

259

260 *4.2.1) Red clays*

261   XRD patterns obtained on the clay fraction of the red clays show a non-expandable phase

262 around 7.1 Å (**Fig. 4A**), which mainly corresponds to the 001 reflexion of kaolinite as this Bragg peak

263 disappears after heating to 550 °C. Chlorite is significantly present in the mixture as evidenced by the

264 003 peak at 4.74 Å, and the slight offset of 004 reflection (3.55 Å) relative to the 002 peak of kaolinite

265 (3.58 Å). The non-expandable peak at 10 Å may suggest the presence of illite, whereas the 14.6 Å peak

266 that expands to 16.8 Å for EG-treated preparations corresponds to swelling smectite. The broad shape

267 in the domain between smectite and illite 001 reflections suggests the presence of interstratified

268 illite/smectite. By focusing on the position of the 060 reflection (**Fig. 4B**), a main broad peak at 1.49-

269 1.50 Å is consistent with the predominance of dioctahedral species like kaolinite and illite, whilst the

270 secondary peak at 1.541-1.543 Å corresponds to a trioctahedral type like chlorite. Quartz and goethite

271 are also present.

272

273 *4.2.2) White clays*

274 XRD patterns of white clays display two identified Bragg peaks at 7.25 Å and 3.61 Å that

275 expand to 7.39 Å and 3.53 Å, respectively, for samples treated with EG (**Fig. 5A**). This indicates the

276 presence of randomly interstratified smectite and of another clay mineral, characterized at 7 Å such as

277 kaolinite or serpentine. This mixed-layered (ML) clay mineral, dominated by the 7 Å phase, coexists

278 with illite and occasional chlorite. Smectite was detected in samples BA130F and BA134F. Associated

279 phases such as cerussite, willemite, ~~goethite~~ and goethite commonly occur. Whilst the broad peak

280 around 1.50 Å, typical of dioctahedral clays corresponds to the position of 060 reflexion of illite, the

281 thin well-defined peak at 1.54 Å suggests a significant proportion of trioctahedral type clay minerals

282 (**Fig. 5B**). Although this may be confused with the 1.541 Å peak due to the 211 reflection of quartz, the

283 060 reflexion patterns are similar between samples which may (e.g. sample BA130F) or may not (e.g.

284 sample BA124F) contain quartz (**Fig. 5A**). For sample BA124, the offset of the broad peak to 1.51 Å is

285 probably an artefact due to a parasite reflexion of zinc silicate (e.g. $11\bar{6}$ for willemite or 530 for

286 hemimorphite).

287

288 *4.2.3) Ochre clays*

289 XRD patterns of the ochre clays do not strongly differ to those of the white clays, with the

290 presence of randomly interstratified smectite and 7 Å mineral (**Fig. 6A**). But the shift of this Bragg

291 peak to lower angular value after EG treatment (up to 7.72 Å and 3.45 Å) suggests a higher smectite

292 proportion in the ML. In addition, illite and smectite are also displayed, as well as cerussite and

293 goethite. The predominance of the trioctahedral type over the dioctahedral type is obviously shown on

294 the 060 reflexion pattern (**Fig. 6B**), with a well-defined thin peak around 1.542 Å and a broad and

295 unclear peak around 1.51 Å, probably polluted by the reflection of minor zinc minerals.

296

297 *4.3) Cation-exchange capacity (CEC) of the different types of clays*

298

299   Although previous observations obtained through XRD measurements have stressed out a

300   possible trend between the type of clays and the amount of Zn content, it does not provide any

301   information on the localization of Zn within the phyllosilicate structure (i.e. in the interlayer space as

302   an exchangeable cations or included in the phyllosilicate sheets). The CEC measurements represent an

303   easy and convenient method allowing one to determine the proportion of exchangeable zinc in the three

304   kinds of clay samples (**Table 2**). The CEC value of the red clays is between 30 and 38 meq/100g,

305   consistent with a mixture of illite, kaolinite and smectite. For 3 out of 4 samples, the amount of

306   exchangeable Zn represents less than 1% of the CEC and is therefore not significant. In contrast, for

307   sample BA121, which may be considered as an exception, more than 40% of the CEC contains

308   exchangeable Zn; this may partly explain the high Zn content (30000 ppm) of this sample, but this

309   assumption is not valid for other mineralized samples such as BA127 (**Table 1**). For the white clays,

310   the CEC values are bracketed between 9 and 27 meq/100g; it may be related to the high content of ML

311   dominated by a non-swelling 7 Å mineral, with a typical CEC value of 5 to 15 meq/100g (**Ma and**

312   **Eggleton 1999**). In the ochre clays, the CEC values may reach 41 meq/100g, as the smectite proportion

313   in the ML is probably higher than in the white clays (**Fig. 6A**). The amount of exchangeable zinc in the

314   CEC is very low for both white and ochre clays, suggesting that zinc is mainly included within the

315   octahedral sites of the clay mineral structure.

316

317   *4.4) Textural observations (OM and SEM)*

318

319   SEM observations of the red clays confirm the presence of a mixture of clay minerals, with

320   dense aggregates of clay platelets (**Fig. 4C**). EDS analyses show that clay minerals are composed of Si,

321   Al, and K, in accordance with the occurrence of illite/kaolinite mixture as identified on XRD patterns

322   (**Fig. 4A**). Isolated laths or sub-euhedral lamella of chlorite are associated to K-rich clays and quartz

323   sub-rounded clasts too (**Fig. 4C**). The bulk clayey matrix displays lighter and porous aggregates of

324   lamella-shaped minerals (**Fig. 4D**); EDS analyses of these patches show Zn enrichment and a low K

325   content relative to the mixture of kaolinite and illite. Descloizite, a zinc vanadate that precipitates under

326   high oxidizing weathering conditions has been locally found (**Fig. 4E**) and may explain, together with

327   the zinc clays, the anomalous high Zn content of some red clayey material samples (e.g. BA121 and

11

328   BA127; **Table 1**). It is worth to notice that no particular phase corresponding to zinc clays was detected

329   by XRD analyses suggesting a low abundance of these zinc-bearing minerals.

330   Optical microscope observations of the white clays show that clay minerals occur in cavity

331   within the ore formed by roundish aggregates of willemite and disseminated galena coated by cerussite

332   (**Fig. 5C**). SEM imaging of the clayey material in these cavities reveals a roughly honeycomb texture

333   of the newly formed clay minerals (**Fig. 5D**). Locally, the micrometre-sized clay sheets are densely

334   aggregated and form patches disseminated in the cavity. EDS analyses reveal that these clays are rich

335   in Zn and poor in K, but sometimes K-rich fragments are found, suggesting an intricate association of

336   both clay types. In most cases, the electronic contrasts between dark K-rich clays and light Zn-rich

337   clays are so clear that it is easy to separate to the related domains, which present a very different

338   textural arrangement (**Fig. 5E**). In the K-rich zone, the illite lamellae coexist with sub-euhedral clasts

339   of quartz. Thin to large bands of Zn-rich clays exposing a honeycomb texture pervade in the cavity and

340   connect to the willemite crystals.

341   Comparable observations can be made in the ochre clayey material, which exposes cavities

342   filled by clay minerals within a primary association of willemite, dolomite and cerussite (**Fig. 6C**). A

343   honeycomb texture of Zn-rich clays analysed by EDS is frequently observed (**Fig. 6D**). In the weakly

344   dense aggregates, the micrometre-sized clay crystals can be individualised, exposing a typical sheeted

345   aspect. Relics of illite lamellae and clasts made of quartz are found isolated in the Zn-rich clay matrix

346   (**Fig. 6E**).

347   The clay minerals and especially the zinc-bearing type are closely associated to willemite;

348   euhedral willemite crystals present evidence of partial dissolution that preferably affects edges or sites

349   of crystalline defect (**Fig. 7A**). Zinc clays may precipitate in this newly formed porosity (**Fig. 7B**), but

350   are mainly found as flakes or platelets either within the K-rich clayey material composed by illite,

351   kaolinite and chlorite (**Fig. 7C**) or along cleavage cracks to form mineralized ribbons (**Fig. 7D**) that

352   fossilized the paths of reactive waters. The honeycomb texture of newly formed zinc clays is frequent

353   in the core of the domain, whereas the clay sheets appear squeezed at the interface with willemite

354   (**Figs. 5E and 7E**). Together with the euhedral shape of the willemite crystal and the evidence of

355   successive rims of willemite, this supports the crystallization of a second generation of willemite

356   (willemite II in **Fig. 7F**) after the formation of the Zn-rich clays.

357

4.4) Microprobe analyses of clay minerals

359

360   WDS quantitative measurements have been carried out on clay aggregates from white and

361 ochre types (samples BA02, BA05 and BA05) and the results are reported in **Table 3**. Only data with a

362 total over 80 %wt, consistent with the range of expected zinc clays minerals (fraipontite, sauconite)

363 have been retained for discussion. The ZnO content, between 1.86 % and 49.39 % appears negatively

364 correlated to the K_2O content varying from 10.01 % to 0.05 %. Similarly, the SiO_2 and Al_2O_3 contents

365 decrease with K_2O. Ca, Fe, Mg and Pb cations are present in minor amount and we observe ~~show~~ slight

366 variations without any relationships with other major elements. Several groups depending on their ZnO

367 and K_2O content and their total oxide content have been distinguished (**Table 3**).

368   For K-rich clayey material, structural formulae were calculated for 22 negative charges (**Table**

369 **3**). For analyses 10, 57 and 58, the number of octahedral cations is around 2 and the number of

370 interlayered cations reaches 0.8, consistent with the occurrence of illite. Analyses 19, 20, 29 and 38

371 show a significant K_2O content (around 2 %) and Zn enrichment up to 30 %; they present a total of

372 analysed oxides around 84 % consistent with pure Zn smectite, i.e. sauconite (**Table 3**). For seven

373 individuals analyses that present a total of analysed oxides around 93 % and a K_2O content between 0.2

374 % and 0.6 %, structural formulae were calculated for 22 negative charges assuming a T-O clay mineral

375 structure. The number of cations in octahedral sites is around 5.5 attesting that the analysed particles

376 are trioctahedral Zn-rich T-O minerals such as fraipontite. The value of M^+ (M^+=K+2Ca) is

377 significantly high, and may mirror surface adsorption of alkaline cations. The 17 remaining analyses

378 display a total oxide between 84 % and 93 % and/or a variable content in K_2O; they probably

379 correspond to a mixture of the above-mentioned end-member clay minerals. The structural formulae

380 calculations were based on 22 negative charges. One can notice the number of cations in the octahedral

381 sites (3.4-3.5) largely exceed the ideal value of 3 (**Table 3**).

382

383 **5) Discussion**

384

385 *5.1) Identification of the nature of Zn clays*

386

387   The results obtained from microscopic observation and XRD analysis, suggest the presence of

388   Zn-bearing clays in the three types of clayey material at Bou Arhous mine, especially in the white and

389   ochre types. By comparing the results given by the two methods, we can deduce that the zinc-rich

390   sheeted aggregates disseminated in the samples correspond to a 7 Å mineral locally interstratified with

391   smectite sheets. In the literature, several types of zinc clays have been described. Sauconite, a

392   trioctahedral smectite close to saponite is the most described clay type and was reported in several

393   deposits in Northern America (**Ross 1946**), Peru (**Boni et al. 2009a**), Southern Africa (**Kärner 2006;**

394   **Terraciano 2008**; **Boni et al. 2011**) and Iran (**Daliran et al. 2009**). Fraipontite (also known as

395   zinalcite), a zincian berthierine (7 Å mineral) has been found in supergene zinc deposits in Belgium

396   (**Fransolet and Bourguignon 1975**), Iberia (**Calvo et al. 2007; Will et al. 2014**), Italy (**Merlino and**

397   **Orlandi 2001**) and Kazakhstan (**Chukhrov 1968**). Other rare zinc clays are Zn-rich beidellite

398   (**Mondillo et al. 2014**), baileychlore, a zinc chlorite (**Rule and Radke 1988**) and hendricksite, a zinc

399   mica (**Frondel and Ito 1966; Robert and Gaspérin 1985**), the latter two occurring in hypogene

400   environments. Besides, moresnetite (**Ross 1946**) and vanuxemite (**Frondel 1972**) have been described

401   as a mixture of zinciferous clays and hemimorphite. No zinc-bearing mixed-layered (ML) minerals

402   have been described, except for illite-zincian smectite ML in Peru (**Mondillo et al. 2014**).

403   In this study, the WDS compositions of the clay crystals show a negative correlation between

404   K (as well as Al and Si) and Zn, suggesting phase mixing at site of analysis (**Table 3**). This is in

405   agreement with the microscopic observation that supports an intricate association between the K-rich

406   and the Zn-rich clays. In the M^+ - 4Si - $3R^{2+}$ ternary plot, classically used for distinguishing the

407   dioctahedral and the trioctahedral types (**Meunier 2005**), our data are scattered along a mixing line that

408   joins the mica pole and the most frequent Zn-clays, namely sauconite and fraipontite (**Fig. 8**). The data

409   corresponding to the purest Zn-clays do not fall into fields of natural sauconite or fraipontite collected

410   in Peru (**Boni et al. 2009a; 2009b**), in Namibia (**Kärner et al. 2006**), in the USA (**Ross 1946**), in UK

411   (**Young et al. 1992**) and in Belgium (**Fransolet and Bourguignon 1975**); data rather fall into an

412   intermediate domain between the theoretical compositions of sauconite and fraipontite. Together with

413   the difficulty of calculating pure sauconite or fraipontite structural formula from our analyses (**Table**

414   **3**), this indicates that our zinc clayey material is dominantly a mixture of fraipontite and sauconite, in

415   agreement with the occurrence of interstratified smectite and 7 Å mineral.

416   Numerical modelling of XRD patterns using the Newmod © program (**Reynolds 1985**) have

417   been carried out to determine the relative proportions of fraipontite and sauconite in the ML mineral.

418   Assuming 1) a mixture of a two-water-layer tri-smectite and a 7 Å mineral, 2) the *00l* reflexions given

419   by Faust (**1951**) and Fransolet and Bourguignon (**1975**), and 3) a Reichweite value of 0, we have

420   produced the XRD patterns presented in **Figure 9**. In this calculation, we have neglected the minor

421   effects of Zn^{2+} on the geometry of ML structure and therefore on the theoretical positions of 00l

422   reflexions. The best simulation to describe the measured XRD pattern is obtained for a mixture

423   containing 80% of fraipontite and 20% of sauconite, namely R0 fraipontite (0.8)/sauconite (**Fig. 9**). To

424   validate this composition, we have recalculated the structural formula assuming a mixing of sauconite

425   and fraipontite at a ratio of 1:4. Based on 39O, the sum of cations in the octahedral sheets is between

426   14.2 and 15 for low K_2O individual data; this value, slightly lower than the ideal value of 15 for the

427   trioctahedral type corroborates the hypothesis of R0 fraipontite(0.8)/sauconite mixed-layered mineral

428   as the zinc-bearing clay mineral. Although such composition of interstratified mineral has never been

429   reported in the literature, the occurrence of the sauconite-fraipontite association has been described in

430   several natural examples of supergene non-sulphide zinc deposits (**Foord et al. 1983**; **Young et al.**

431   **1992**; **Maltsev and Korshunov 1988**), or even found in experimental works (**Esquivin 1957; 1960**).

432

433   *5.2) Genetic processes accounting for Zn-clays formation*

434

435   Results obtained on whole-rock samples show the difficulty of identifying significant differences

436   between the three types of clayey material to understand their genetic link with the ore and the host

437   rock. Despite these difficulties, the following implications may be deduced from the above-mentioned

438   analysis:

439   - Dolomite is present in the Jurassic limestone and in the gangue of Zn-Pb ore. Its occurrence

440   in the ochre and white clayey materials and its relative absence in the red one may indicate different

441   genetic processes accounting for their respective origin.

442   - Microscope observations have shown that Zn-clays are very frequently associated to detrital

443   illite, which is dominant in the red clayey material. Zinc enrichment of clay minerals in the white and

444   ochre clayey materials is consistent with the neogenesis of mixed layered fraipontite(0.8)/sauconite

445   minerals, requiring sources for zinc, silica and aluminium.

15

446   - The main zinc-bearing mineral at Bou Arhous is willemite, whose conditions of formation

447   remain unclear (**Choulet et al. 2014**). It may have been formed under supergene conditions as

448   exemplified by the deposits in Nevada (**Takahashi 1960**), or in Zambia (**Terraciano 2008**).

449   Alternatively, a hydrothermal or hypogene origin for willemite (**Brugger et al. 2003**; **Hitzmann et al.**

450   **2003, Boni et al. 2011**) could be envisaged, but no field and mineralogical observations are currently

451   supporting this hypothesis.

452   The origin of willemite in such supergene environment is not clearly understood as this

453   mineral is mostly described in hypogene or hydrothermal deposits (**Hitzman et al. 2003**; **Coppola et**

454   **al. 2008**). Its occurrence at Bou Arhous may suggest either a low-temperature hydrothermal stage or

455   exceptional physico-chemical conditions characterised by a combination of high silica activity, low

456   $P(CO_2)_g$, alkaline conditions and oxidizing environment (**Choulet et al. 2014**). At 25°C, willemite may

457   be partly dissolved by meteoric waters rich in Ca and poor in Si (**Brugger et al. 2003**); such conditions

458   are reached in karst environment because of water-host rock interaction. This can explain the evidence

459   for supergene dissolution of willemite, releasing Zn and Si in the solution (**Figs. 7A and 7B**). This

460   dissolution is probably congruent as no quartz or silica gel, incorporating the silicon in excess, remains

461   or precipitates in the secondary porosity. The addition of Zn and Si ions in the solution changes

462   equilibrium and the solubility of the Zn-bearing phases strongly depends on the pH conditions

463   (**Takahashi 1960**; **Brugger et al. 2003**). As no smithsonite or hydrozincite precipitation has been

464   observed in our samples despite high $P(CO_2)_g$ due to karst buffering, slightly acid (ca. 5) conditions

465   must be envisaged to transport the Zn^{2+} ions as chlorozinc(II) complexes (**Ruaya and Seward 1986**)

466   and to enable a further precipitation of zinc clays. The absence of widespread hemimorphite is difficult

467   to understand, as this phase is supposed to precipitate under acid pH conditions and relatively high

468   silica activity (**Takahashi 1960**; **McPhail et al. 2003**); however, this may be explained by the limited

469   field of hemimorphite stability and its sensibility to strong $P(CO_2)_g$ variations (**Reichert and Borg**

470   **2008**).

471   The availability of Al is also critical for the neogenesis of the Zn clays, and requires a local

472   source because of the low mobility of Al in meteoric waters. The Zn clays are often associated to the

473   K-rich clays, mainly illite as evidenced by the XRD patterns of the white and ochre clayey materials.

474   At the scale of the cavity, the pervasion of the Zn-rich clays in the material dominated by the K-rich

475   clays shall suggest a pseudomorphosis of primary illite and smectite and their replacement by the

16

476 mixed-layered clay minerals (**Figs. 5D or 6E**). The very close association of illite and Zn clays

477 suggests that partial dissolution of external illite layers, due to hydrolysis and the break up of Al-O and

478 Si-O bonds, contributes to releasing Al and Si, further incorporated in the newly formed ML clay

479 minerals. The Zn clays may also pseudomorph after dissolved willemite (**Fig. 7B**), but this requires a

480 close source for Al.

481   In karstic environments, the physico-chemical conditions of meteoric waters continuously

482 change due to carbonate buffering. A rapid increase of pH causes tremendous variations of the

483 solubility of zinc silicates like willemite that can further precipitate even at surface temperature and

484 under neutral conditions (**Brugger et al. 2003**). This precipitation of secondary willemite (Willemite

485 II) forming euhedral rim around primary willemite (willemite I) leads to squeezing of newly formed

486 zinc clays (**Fig. 7E and 7F**). As a consequence, the honeycomb texture is locally erased, and jamming

487 contributes to emphasize the very fine mixing between illite and ML clay minerals (**Fig. 7E**).

488 Secondary willemite also occurs as idiomorphic crystals in the open space of the clayey cavities (**Fig.

489 7D**) or as infilling material within fractures of primary willemite (**Fig. 7F**).

490

491 *5.3) Conditions for Zn mineralisation of clays and relation to the ore evolution*

492

493   The mechanisms of Zn-rich clays formation have been rarely reported in the literature. In Zn

494 ore deposits of Peru, Boni et al. (**2009a**) have identified sauconite and altered feldspars and they

495 proposed that sauconite in silicoclastic host rocks may result from interaction between feldspar

496 weathering and Zn-rich solution derived from supergene dissolution of zinc sulphide. At Abenab West

497 ore deposit (Namibia), hosted in limestone, a progressive enrichment in Zn and Mg of barren clays is

498 suggested, but details of the nature of zinc clays and the processes related to their neogenesis are

499 presently not available (**Terraciano 2008**).

500   Like Abenab West ore deposit, zinc ore at Bou Arhous is hosted in limestone that has

501 developed a large karst network since its exhumation at surface (**Leblanc 1968**). The Bou Arhous karst

502 presents some non-dissolved material concentrated in various-sized cavities. Field observations have

503 shown that this red clayey material is composed by a fine succession of silt and clay horizons that

504 present sedimentation features. The red clay type may correspond to "residual" clays, which generally

505 show mixing components between detrital sources and insoluble parts of the dissolved limestone

506 (**Chamley 1989**). The residual red clays are composed of clay minerals like illite, chlorite, kaolinite

507 and smectite, iron oxi-hydroxide and quartz. This composition is somehow similar to that of the

508 classical peri-Mediterranean karst-related clayey infilling, known as *terra rossa*, that shows stratiform

509 accumulation of red clayey material in cavity formed after limestone dissolution (e.g. **Blanc and**

510 **Chamley 1975**; **Moresi and Mongelli 1988**; **Iacoviello and Martini 2013**).

511 The red clays are originally barren (**Table 1**), but may be fertilized by several complementary

512 processes that includes:

513 - Sedimentary recycling of zinc ore fragments, such as willemite (**Figs. 3C and 3D**).

514 - Precipitation of newly formed zinc-bearing minerals like descloizite (**Fig. 4E**), which is

515 typical of high oxidising supergene environment (**Boni et al. 2007**).

516 - Adsorption of the Zn^{2+} cations at the clay surface or fixing of the Zn^{2+} cations in the

517 interlayer, as indicated by the amount of $[Zn^{2+}]$ released after the CEC measurements (**Table 2**). This

518 process is well known in the literature as many studies have focused on the capacity of clays to trap

519 heavy metals like Zn (e.g. **Bradbury and Baeyens 1999**; **Dähn et al. 2011**).

520 - Precipitation of the Zn-rich clays in small-disseminated patches (**Fig. 4D**), up to large

521 pervasion (**Figs. 5D and 6E**) in the red detrital clayey material. This process is able to progressively

522 form the white or the ochre clays found in the Bou Arhous deposit. As seen earlier, this process is

523 characterized by the neogenesis of authigenic clay minerals that nucleate on micas. It may be compared

524 to the epitaxial growth of Zn clays on smectites, which interacts with a solution enriched in Zn and Si

525 (**Schlegel et al. 2001; Schlegel and Manceau 2006**). These authors reported newly formed clays as a

526 mixture of Zn-saturated TO and TOT trioctahedral phyllosilicates, thereby presenting lot of similarities

527 with the R0 fraipontite(0.8)/sauconite mixed-layered mineral identified in this study. The presence of a

528 clay precursor for nucleation and Al supply is required for the neogenesis of Zn-clays, which also

529 depends on the silica activity (**Schlegel et al. 2001**). At low Si concentration, Zn may be fixed in

530 polymer chains in structural continuity to the smectite. High Si concentration rather facilitates the

531 neogenesis of authigenic clays and especially the formation of Zn-rich TO phyllosilicates, such as

532 fraipontite. Other experimental studies at supergene conditions have showed that the presence of Al

533 may play a role for the type of clay that precipitates (**Tiller and Pickering 1974**), with 2:1 layer

534 silicate in Al-free conditions and, in the presence of aluminium, formation of 1:1 layer silicate similar

535 to Zn berthierine, a synthetic product equivalent to fraipontite (**Esquevin 1960**). Such chemical

536   controls could be hypothesised to spell out the different types of Zn clays met throughout the world.

537   The climate dependence classically evoked for the variability of clay types (**Chamley 1989**) may also

538   be taken into account, but its role is currently difficult to understand, given the scarcity of reliable data

539   on Zn clay occurrences.

540   The formation of zinc clays at Bou Arhous is a continuous process during the late supergene

541   evolution of the ore deposit. Initially, zinc was included in sulphide lenses hosted in the Lower Jurassic

542   limestone (**Leblanc 1968**). The regional uplift and the folding episode related to the Atlas tectonics

543   during the Tertiary have led to an exhumation of the sulphide ore and a verticalisation of the limestone

544   strata (**Choulet et al. 2014**). As a consequence, the meteoric water has percolated in the fractures and

545   has provoked the dissolution of the limestone and the oxidation of the sulphides. For some unclear

546   reasons, zinc has first re-precipitated as willemite, forming a "black ore" due to its association with

547   preserved galena and cerussite. Willemite has further interacted with karstic waters, probably poor in Si

548   and slightly acid, leading to its partial dissolution and to releasing of Zn and Si in the solution (**Fig.**

549   **10**). In parallel, the development of a karst was characterised by the opening of various-sized

550   dissolution cavities filled by detrital supplies and insoluble materials (**Fig. 10**). At surface conditions,

551   this red clayey material has been pervaded by Zn-Si-rich solutions resulting in the neogenesis of Zn-

552   clays (mixed-layered clay minerals) that nucleate on detrital micas. At site of zinc ore concentration,

553   red clays were progressively transformed into white and ocher clays. The further crystallisation of late

554   generations of willemite indicates that this process is continuous in time, highly dependant on the

555   chemistry and dynamics of karstic solutions, and therefore difficult to timely constrain in the ore

556   deposit evolution.

557

558   **6) Conclusion**

559

560   This study has revealed the nature of the zinc clays at Bou Arhous deposit and the

561   mechanisms called for their genesis. Although several processes are involved for the metal enrichment

562   of barren clays, the crystallisation of Zn clays appears to be the major one. This neogenesis is related to

563   the interaction between Zn-rich meteoric water and residual clays related to karst evolution. This model

564   has strong implication for the mineral industry, as Zn-rich clayey material grading up to 30% Zn is a

565   non-negligible resource that may be easily identified. The target zones will be the karst cavities located

566   around the original ore body (potentially dissolved); residual clays must fill these cavities, representing

567   the necessary condition for the nucleation of the newly formed clay crystals. The soft nature of the

568   clayey material could probably facilitate mining, at least in case of open-pit extraction, and especially

569   contributes to costs reduction in the early operations.

570   Conversely, by deciphering the mineralogical nature of the Zn-rich clayey material, this study

571   has showed the mixture of authigenic mixed-layered clays and detrital phyllosilicates. Except for rare

572   samples, zinc cannot be recovered easily as it is located within the octahedral sites in each component

573   of the interstratified mineral. Consequently, Zn can only be released by leaching techniques such as

574   solvent extraction, which is relatively efficient for a given clay species like sauconite (**Boni et al.**

575   **2009b**). But, in the presence of interstratified minerals finely disseminated within detrital barren clays,

576   ore liberation may be more difficult and requires advances for 1) an efficient separation between barren

577   and mineralised clays, and 2) a better selectivity of solvents used. Another consequence of this intricate

578   mineralogical association is the excess of barren materials that need to be handled and processed,

579   thereby representing a major limitation to the economic potential of zinc clays.

580

589

590   **Figure Captions**

591

592   **Fig. 1** a: Simplified tectonic map of Morocco. b: Geological map of the Bou Arhous range. c: Cross-

593   Section across the Bou Arhous range, showing the structural and stratigraphic location of the ore

594   deposit (modified after **Choulet et al. 2014**)

595

596 **Fig. 2** a: Non-sulphide ore veins cropping out at the surface. b: Lower Jurassic host rock composed of

597 limestone and marl strata. c: Triassic variegated shale inside the mine. d: Preserved sulphide associated

598 to calcite and willemite in a "black ore" vein. e: Illustration of the different types of clayey material

599 with relationships to "black ore"

600

601 **Fig. 3** a: Association of red clays and white to ochre clays inside the mine. b and c: Details of the

602 interconnected karst cavities, filled by red clayey material showing shallow inclined bedding. d: White

603 clays at the interface between the black ore and the red clays. e: Large occurrence of white clays

604 around black ore. f: Cavity filled by ochre clays spotted by relics of black ore

605

606 **Fig. 4** a: XRD patterns of representative samples of red clayey material (oriented clay fraction

607 preparation). See text for details about Bragg peaks indexation. Black (red) curves were obtained in dry

608 (Ethylene glycol (EG)) conditions. Sm: smectite, K: kaolinite, Ill: illite, Chl: chlorite, Qz: quartz, Goe:

609 goethite. b: XRD patterns (misoriented clay fraction preparation) emphasizing the position of 060

610 reflections for representative samples of red clayey material. c to e: BSE images of red clays

611 illustrating the detrital origin of this material that contains a mixture of chlorite, illite, smectite, quartz

612 clasts and secondary Zn-rich mineral patches

613

614 **Fig. 5** a: XRD patterns of representative samples of white clayey material (oriented clay fraction

615 preparation) Sm: smectite, Ill: illite, ML: mixed-layers, Will: willemite, Cc: cerusite, Qz: quartz. b:

616 XRD patterns (misoriented clay fraction preparation) emphasizing the position of 060 reflections for

617 representative samples of white clayey material. c: Illustration of cavities filled with white clays inside

618 the black ore (transmitted light, crossed nichols). d: BSE image of the mixture of Zn-rich clays and K-

619 rich clays, with light grey patches composed by Zn-rich clays. e: BSE image of zinc clays aggregate in

620 cavities filled by detrital clays and relationships between clays and willemite crystals

621

622 **Fig. 6** a: XRD patterns of representative samples of ochre clayey material (oriented clay fraction

623 preparation) Sm: smectite, Ill: illite, ML: mixed-layers, Will: willemite, Qz: quartz; b: XRD patterns

624 (misoriented clay fraction preparation) emphasizing the position of 060 reflections for representative

625 samples of ochre clayey material. c to e: BSE images of the ochre clayey material. c: relationships

626   between zinc clays and ore and gangue minerals (willemite, cerussite and dolomite). d and e: Detailed

627   view of the zinc clays, with disseminated relics of detrital micas and quartz

628

629   **Fig. 7** Secondary (a and f) and back-scattered (b to e) electron images of willemite and zinc clays in

630   black ore and white to ochre clay samples. a: partially dissolved willemite crystal with clay particles on

631   its surface. b: Neogenesis of authigenic zinc clays that precipitate in the void created by the partial

632   dissolution of a willemite crystal. c: Newly formed zinc clays flakes precipitating on detrital micas

633   surfaces. d: Ribbon-like aggregates of zinc clays filling the space between detrital clays. Note the

634   precipitation of late euhedral willemite crystals (willemite II) in the porosity. e: Pervasive enrichment

635   in zinc clays of a geode initially filled by detrital clays. Note the idiomorphic willemite crystals close to

636   squeezed zinc clays; this crushed texture suggests willemite growth after zinc clays formation. f:

637   Polyphase crystallization of willemite, showing growth zoning and fracture infilling

638

639   **Fig. 8** $4Si-M^+-3R^{2+}$ diagram, illustrating the mixture of di- and tri-octahedral end-members. Our data

640   are plotted as square symbols and are compared with data reported in the literature. Colour assignment

641   matches the different types as showed in Table 3. Red: mica, green: fraipontite, blue: sauconite and

642   black: mixture of these three end-members

643

644   **Fig. 9** Calculated XRD patterns given by Newmod modelling. Black (red) curves were obtained in dry

645   (Ethylene glycol (EG)) conditions. See text for data inputs and implications

646

647   **Fig. 10** Schematic view illustrating the formation of zinc clays in a mineralised karstic environment.

648   The relationships between the black ore (supergene non-sulphide ore) and the residual clays are

649   emphasized. The two BSE images show the detrital texture of red clays before zinc mineralisation

650   (right) and the honeycomb texture of white to ochre clays after neogenesis of zinc clays (left)

651

652   **Table 1** Sampling details of the host rocks and clayey material, with bulk mineralogy deduced from

653   XRD and geochemical content obtained by ICPMS analyses. Abbreviations: cc: calcite, ce: cerussite,

654   cl: clays, do: dolomite, ga: galena, goe: goethite, gy: gypsum, he: hematite, qtz: quartz

655

656　**Table 2** Values of the CEC and zinc content of the CEC for the three types of clay materials reported

657　in this study. The clay content is deduced from XRD analyses and is illustrated in figs 4 to 6

658

659　**Table 3** WDS results and calculated structural formulae for the different types of clay minerals and

660　aggregates. See text for explanation about calculation and data sorting

661

662　**References**

663

664　Abkhoshk E, Jorjani E, Al-Harahsheh MS, et al (2014) Review of the hydrometallurgical processing of

665　　　non-sulfide zinc ores. Hydrometal 149:153–167. doi: 10.1016/j.hydromet.2014.08.001

666　Ammann L, Bergaya F, Lagaly G (2005) Determination of the cation exchange capacity of clays with

667　　　copper complexes revisited. Clay Minerals 40:441–453. doi: 10.1180/0009855054040182

668　Bayraktar I, Aslan A, Ersayin S (1998) Effects of primary slime and clay on selectivity of flotation of

669　　　sub-volcanogenic complex polymetallic ores. Trans Instit Min Metal Sect B Applied Earth Sci

670　　　107:C71–C76

671　Blanc J, Chamley H (1975) Remplissages de réseaux karstiques à la grotte de Saint-Marcel d'Ardèche.

672　　　Quaternary 12:71–82. doi: 10.3406/quate.1975.2084 (in French)

673　Boni M, Large D (2003) Nonsulfide Zinc Mineralization in Europe: An Overview. Econ Geol 98:715–

674　　　729. doi: 10.2113/gsecongeo.98.4.715

675　Boni M, Terracciano R, Evans NJ, et al (2007) Genesis of Vanadium Ores in the Otavi Mountainland,

676　　　Namibia. Econ Geol 102:441–469. doi: 10.2113/gsecongeo.102.3.441

677　Boni M, Balassone G, Arseneau V, Schmidt P (2009a) The Nonsulfide Zinc Deposit at Accha

678　　　(Southern Peru): Geological and Mineralogical Characterization. Econ Geol 104:267–289. doi:

679　　　10.2113/gsecongeo.104.2.267

680　Boni M, Schmidt PR, De Wet JR, et al (2009b) Mineralogical signature of nonsulfide zinc ores at

681　　　Accha (Peru): A key for recovery. Int J Mineral Processing 93:267–277. doi:

682　　　10.1016/j.minpro.2009.10.003

683　Boni M, Terracciano R, Balassone G, et al (2011) The carbonate-hosted willemite prospects of the

684　　　Zambezi Metamorphic Belt (Zambia). Miner Deposita 46:707–729. doi: 10.1007/s00126-011-0338-

685　　　7.

686   Bradbury MH, Baeyens B (1999) Modelling the sorption of Zn and Ni on Ca-montmorillonite. Geoch

687   Cosmoch Acta 63:325–336. doi: 10.1016/S0016-7037(98)00281-6

688   Brugger J, McPhail DC, Wallace M, Waters J (2003) Formation of Willemite in Hydrothermal

689   Environments. Econ Geol 98:819–835. doi: 10.2113/gsecongeo.98.4.819

690   Calvo M, Viñals J, Triviño A (2007) Zálesiíte, felsobanyaite and fraipontite, in a conglomerate in

691   Prullans, La Cerdanya, Catalonia (Spain). Mineral Up I:49–51

692   Chamley H (1989) Clay sedimentology. Springer-Verlag, Berlin Heidelberg

693   Choulet F, Charles N, Barbanson L, et al (2014) Non-sulfide zinc deposits of the Moroccan High Atlas:

694   Multi-scale   characterization   and   origin.   Ore   Geol   Rev   56:115–140.   doi:

695   10.1016/j.oregeorev.2013.08.015

696   Chukhrov FV (1968) Some Results of the Study of Clay Minerals in the U.S.S.R. Clays and Clay

697   Minerals 16:3–14. doi: 10.1346/CCMN.1968.0160103

698   Churakov SV, Dähn R (2012) Zinc Adsorption on Clays Inferred from Atomistic Simulations and

699   EXAFS Spectroscopy. Environ Sci Technol 46:5713–5719. doi: 10.1021/es204423k

700   Connelly (2011) High clay ores: a mineral processing nightmare part 2. Australian J Mining 4

701   Coppola V, Boni M, Gilg HA, et al (2008) The "calamine" nonsulfide Zn–Pb deposits of Belgium:

702   Petrographical, mineralogical and geochemical characterization. Ore Geol Rev 33:187–210. doi:

703   10.1016/j.oregeorev.2006.03.005

704   Crundwell F, Moats M, Ramachandran V, et al (2011) Extractive Metallurgy of Nickel, Cobalt and

705   Platinum Group Metals. Elsevier, Oxford

706   Dähn R, Baeyens B, Bradbury MH (2011) Investigation of the different binding edge sites for Zn on

707   montmorillonite using P-EXAFS – The strong/weak site concept in the 2SPNE SC/CE sorption

708   model. Geoch Cosmoch Acta 75:5154–5168. doi: 10.1016/j.gca.2011.06.025

709   Daliran F, Armstrong R, Borg G, et al (2009) Nonsulphide Zinc Deposits, Iran - The Hypogene

710   Emplacement and Supergene Modification History of the Angouran Zinc Deposit, NW-Iran.

711   Bundesanstalt für Geowissenschaften und Rohstoffe

712   De Wet JR, Singleton JD (2008) Development of a viable process for the recovery of zinc from oxide

713   ores. J South Afr Instit Mining Metal 108:253

714   Esquevin J (1957) Sur la composition minéralogique des moresnétites et l'existence probable d'une

715   nouvelle phyllite zincifère. Comptes Rendus de l'Académie des Sciences (Paris) A/3150:4022. (in

716   French)

717   Esquevin J (1960) Les Silicates de zinc, étude de produits de synthèse et des minéraux naturels. Institut

718   national de la recherche agronomique, Saint-Amand (in French)

719   Faust GT (1951) Thermal analysis and X-ray studies of sauconite and of some zinc minerals of the

720   same paragenetic association. Am Mineral 36:795–822

721   Foord EE, Taggart JE, Conklin NM (1983) Cuprian fraipontite and sauconite from the Defiance-Silver

722   Bill mines, Gleeson, Arizona. Mineral Record 14:131–132

723   Fransolet A-M, Bourguignon P (1975) Données nouvelles sur la fraipontite de Moresnet (Belgique).

724   Bull Soc Fr Mineral 98:235–244

725   Frizon de Lamotte D, Leturmy P, Missenard Y, et al (2009) Mesozoic and Cenozoic vertical

726   movements in the Atlas system (Algeria, Morocco, Tunisia): An overview. Tectonophysics 475:9–

727   28. doi: 10.1016/j.tecto.2008.10.024

728   Frondel C (1972) The minerals of Franklin and Sterling Hill, a checklist. Wiley-Interscience, New

729   York

730   Frondel C, Ito J (1966) Hendricksite, a new species of mica. Am Mineral 51:1107–1123

731   Fuerstenau MC, Jameson GJ, Yoon R-H (2007) Froth Flotation: A Century of Innovation. SME,

732   Englewood

733   Gaudefroy C (1959) Kaolinite et montmorillonite zincifères (sauconite?) d'Iboughalène. Not Mem du

734   Serv Geol Maroc 144:152–153

735   Gnoinski J (2007) Skorpion Zinc: optimization and innovation. J South Afr Instit Mining Metal

736   107:657–662

737   Hitzman MW, Reynolds NA, Sangster DF, et al (2003) Classification, Genesis, and Exploration Guides

738   for Nonsulfide Zinc Deposits. Econ Geol 98:685–714. doi: 10.2113/gsecongeo.98.4.685

739   Iacoviello F, Martini I (2013) Clay minerals in cave sediments and terra rossa soils in the Montagnola

740   Senese karst massif (Italy). Geol Quarterly 57:527—536

741   Kärner K (2006) The metallogenesis of the Skorpion non-sulphide zinc deposit, Namibia. Dissertation,

742   Univerität Martin Luther

743 Leblanc M (1968) Etude géologique et métallogénique du jbel Bou-Arhous et de son prolongement

744 oriental (Haut Atlas marocian oriental). Not Mem Serv geol Maroc 206:117–206 (in French)

745 Lim J (2011) Controlling clay behaviour in suspension: developing a new paradigm for the minerals

746 industry. Dissertation, University of Melbourne

747 Ma C, Eggleton RA (1999) Cation Exchange Capacity of Kaolinite. Clays and Clay Minerals 47:174–

748 180. doi: 10.1346/CCMN.1999.0470207

749 Maltsev V, Korshunov V (1998) Geochemistry of fluorite and related features of the Kugitangtou

750 Ridge Caves, Turkmenistan. J Caves Karst Stud 60:151–155

751 Mattauer M, Tapponnier P, Proust F (1977) Sur les mecanismes de formation des chaines

752 intracontinentales; l'exemple des chaines atlasiques du Maroc. Bull Soc Geol fr S7-XIX:521–526.

753 doi: 10.2113/gssgfbull.S7-XIX.3.521 (in French)

754 McPhail DC, Summerhayes E, Welch S, Brugger J (2003) The geochemistry and mobility of zinc in

755 the regolith. Cooperative Research Centre for Landscape Environments and Mineral Exploration

756 http://crcleme.org.au/Pubs/Advancesinregolith/AdvancesinRegolith.html.

757 Meier LP, Kahr G (1999) Determination of the Cation Exchange Capacity (CEC) of Clay Minerals

758 Using the Complexes of Copper(II) Ion with Triethylenetetramine and Tetraethylenepentamine.

759 Clays and Clay Minerals 47:386–388. doi: 10.1346/CCMN.1999.0470315

760 Merlino S, Orlandi P (2001) Carraraite and zaccagnaite, two new minerals from the Carrara marble

761 quarries: their chemical compositions, physical properties, and structural features. Am Mineral

762 86:1293–1301

763 Meunier A (2005) Clays. Springer Verlag, Berlin Heidelberg

764 Mondillo N, Nieto F, Balassone G, Boni M (2014) Zn-rich clay minerals in supergene ores (Cuzco

765 area, Peru); a TEM study with inferences for genesis and processing IMA meeting, Johannesburg.

766 Moresi M, Mongelli G (1988) Underlying limestones and dolostones in Apulia, Italy. Clay Minerals

767 23:439–446

768 Newman ACD (1987) Chemistry of clays and clay minerals. Wiley, New-York

769 Reichert J, Borg G (2008) Numerical simulation and a geochemical model of supergene carbonate-

770 hosted non-sulphide zinc deposits. Ore Geol Rev 33:134–151. doi:

771 10.1016/j.oregeorev.2007.02.006

772 Reynolds RCJ (1985) NEWMOD a computer program for the calculation of one-dimensional X-Ray

773   diffraction patterns of mixed-layered clays. Reynolds, R C J, 8 Brook Dr., Hanover, New

774   Hampshire

775 Robert J-L, Gasperin M (1985) Crystal structure refinement of hendricksite, a Zn- and Mn-rich

776   trioctahedral, potassium mica: a contribution to the crystal chemistry of zinc-bearing minerals.

777   Tschermaks Minerale Petrograph Mitteil 34:1–14

778 Ross CS (1946) Sauconite - a clay mineral of the montmorillonite group. Amer. Miner., 31: 411. Am

779   Mineral 31:411–424

780 Ruaya JR, Seward TM (1986) The stability of chlorozinc(II) complexes in hydrothermal solutions up to

781   350°C. Geoch Cosmoch Acta 50:651–661. doi: 10.1016/0016-7037(86)90343-1

782 Rule AC, Radke F (1988) Baileychlore, the Zn end member of the trioctahedral chlorite series. Am

783   Mineral 73:135–139

784 Schlegel ML, Manceau A (2006) Evidence for the nucleation and epitaxial growth of Zn phyllosilicate

785   on montmorillonite. Geoch Cosmoch Acta 70:901–917. doi: 10.1016/j.gca.2005.10.021

786 Schlegel ML, Manceau A, Charlet L, et al (2001) Sorption of metal ions on clay minerals. III.

787   Nucleation and epitaxial growth of Zn phyllosilicate on the edges of hectorite. Geoch Cosmoch

788   Acta 65:4155–4170. doi: 10.1016/S0016-7037(01)00700-1

789 Takahashi T (1960) Supergene alteration of zinc and lead deposits in limestone. Econ Geol 55:1083–

790   1115. doi: 10.2113/gsecongeo.55.6.1083

791 Teixell A, Arboleya M-L, Julivert M, Charroud M (2003) Tectonic shortening and topography in the

792   central High Atlas (Morocco). Tectonics 22:1051. doi: 10.1029/2002TC001460

793 Terracciano R (2008) Willemite Mineralisation in Namibia and Zambia. Dissertation, Università degli

794   Studi di Napoli Federico II

795 Tiller KG, Pickering JG (1974) The Synthesis of Zinc Silicates at 20°C and Atmospheric Pressure.

796   Clays and Clay Minerals 22:409–416. doi: 10.1346/CCMN.1974.0220507

797 Warme JE (1988) Jurassic carbonate facies of the Central and Eastern High Atlas rift, Morocco. In:

798   Jacobshagen PDVH (ed) The Atlas System of Morocco. Springer Berlin Heidelberg, pp 169–199

799 Will P, Friedrich F, Hochleitner R, Gilg HA (2014) Fraipontite in the hydrothermally overprinted

800   oxidation zone of the Preguiça mine, Southern Portugal. Mid-European Clay Conference, Dresde.

801   Young B, Livingstone A, Thomson N (1992) Fraipontite from Wensleydale, North Yorkshire. Proc

802   Yorkshire Geol Soc 49:125–127. doi: 10.1144/pygs.49.2.125

Figure 1
Click here to download Figure: Fig1.tif

a

Atlantic Ocean
Mediterranean Sea   Algiers
Tangier
Alpine Belts   Tell
Rabat   RiF
Middle
Atlas   High Plateau
Moroccan Meseta   Saharan Atlas
High Atlas
Saharan platform
Anti Atlas
0   125   250 km

N

"Grand Accident"
Thrust

Figure 1C

Iboughalene
(Zn) Mine

Bou Arhous
Mine

Atchana
Mine

1 km

b

Quaternary sediments	Limestone (Aalenian)
Marl and limestone (mid-Jurassic)	Marl (Toarcian)
Marl and limestone (Pliensbachian)	

Upper Sinemurian
| Dolomitic limestone | Coral reef | Stratified limestone |

Lower Sinemurian
| Dolomitic limestone | Massive limestone |

| Massive limestone (undifferentiated Sinemurian) | |
| Triassic shales (including gypsum beds) and lavas | |

c

N   S

Bou Arhous
Mine

Figure 2
Click here to download Figure: Fig2.tif

a. Vein of non-sulphide zinc ore; Jurassic Host limestone

b. Marl; Host limestone

c. Triassic variegated shale

d. Host limestone; Calcite; Galena + willemite; 10 cm

e. Ochre clays; Red clays; Galena + willemite; White clays
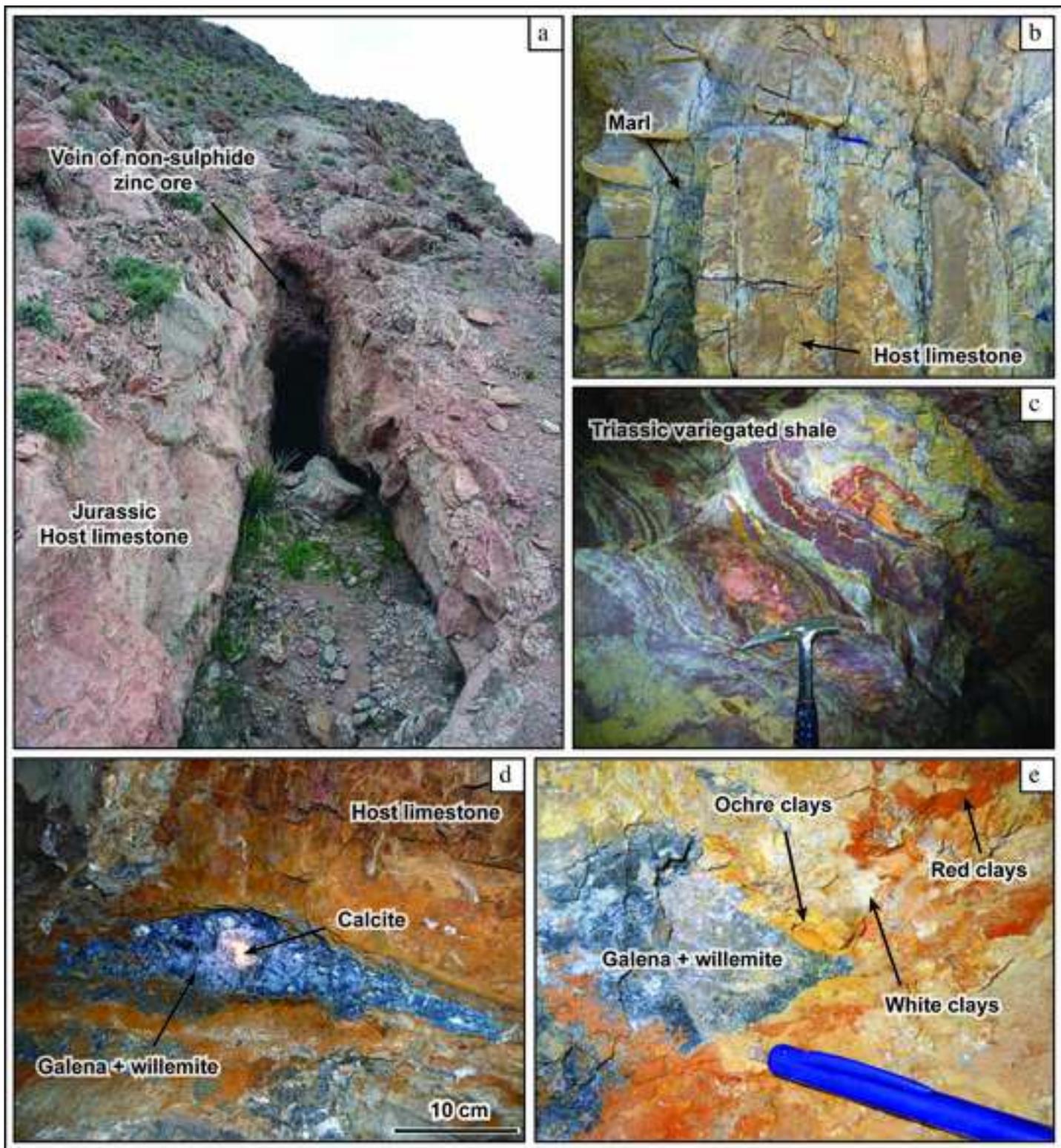
Figure 3
Click here to download Figure: Fig3.tif
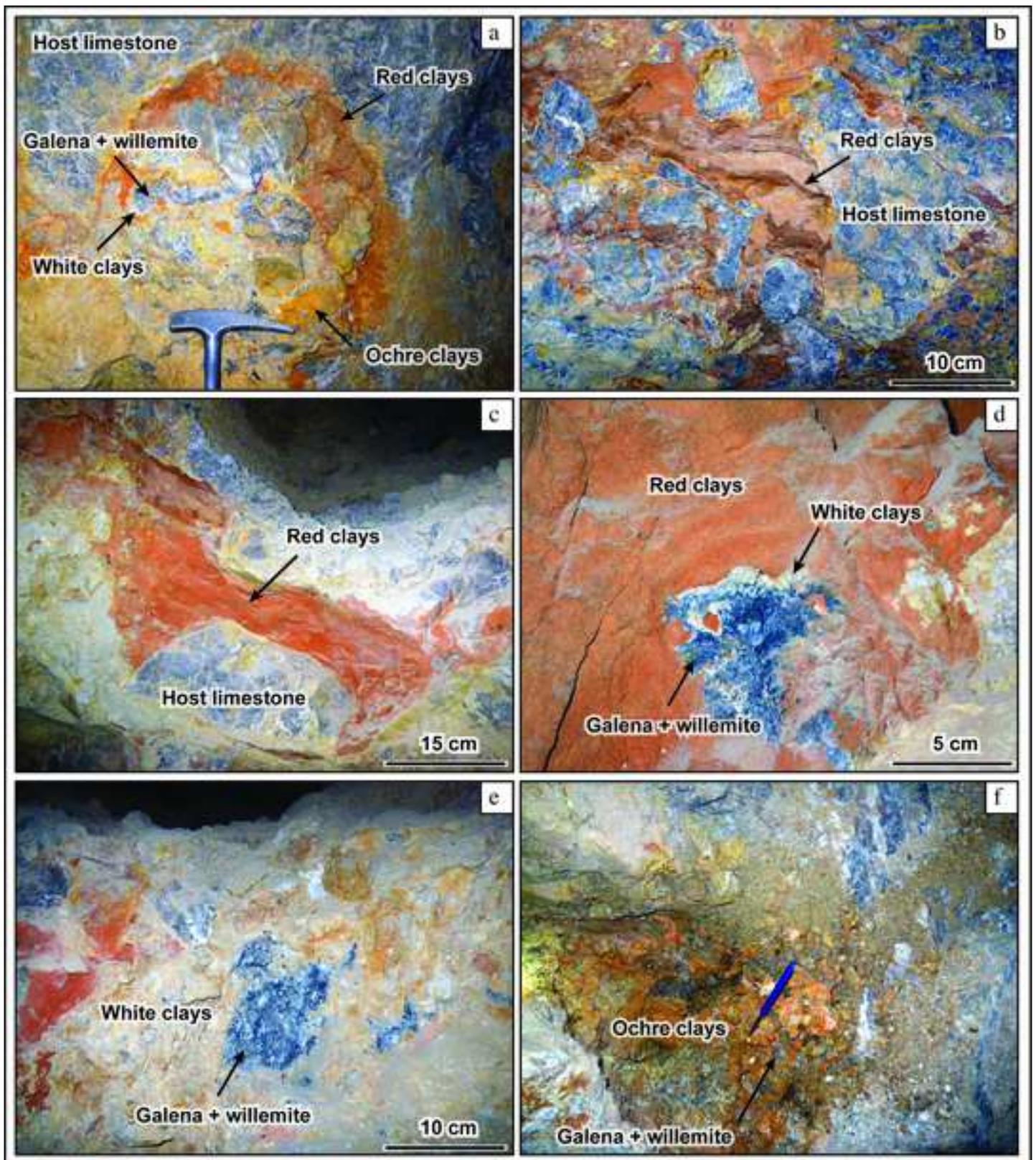
Figure 3
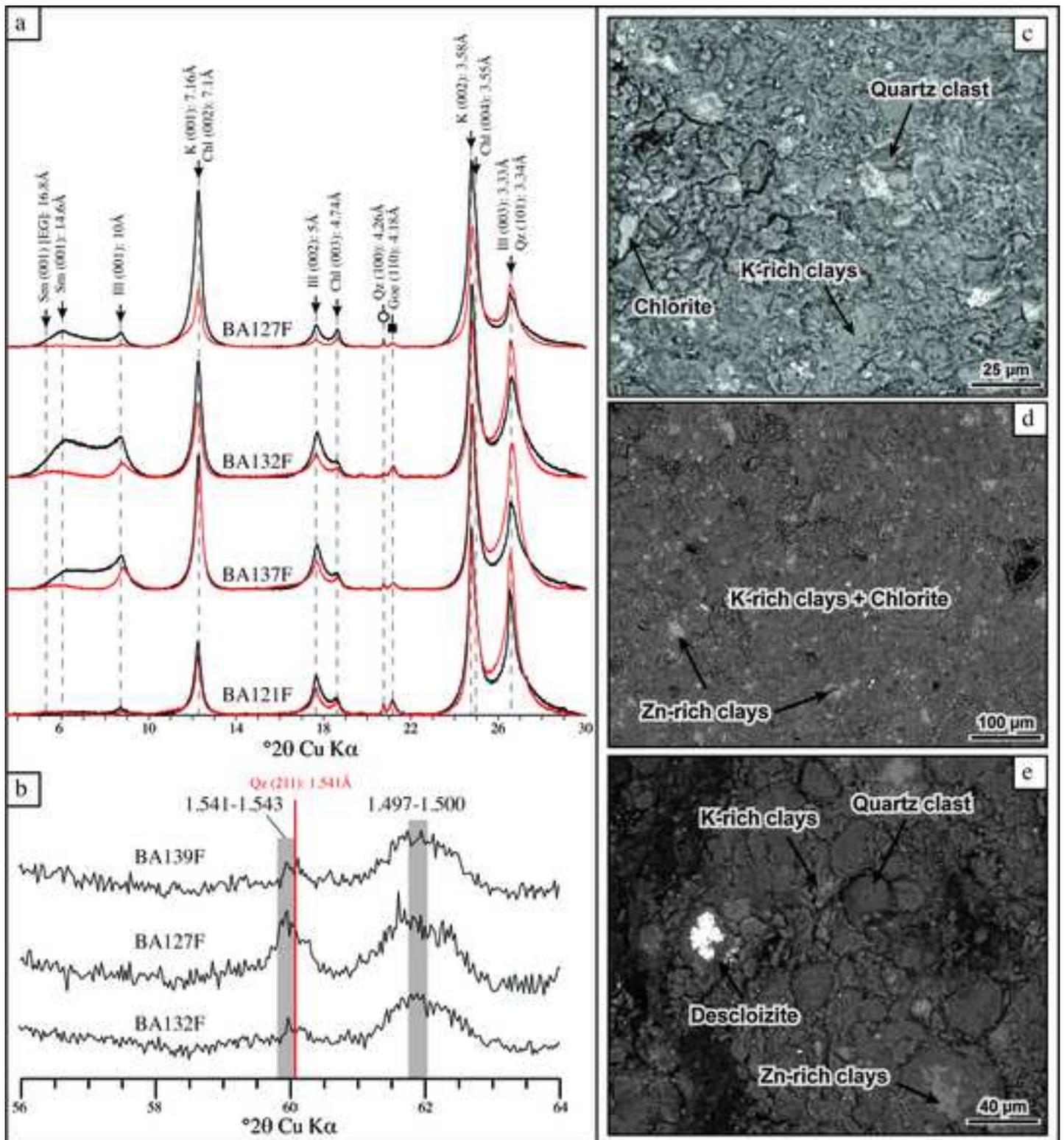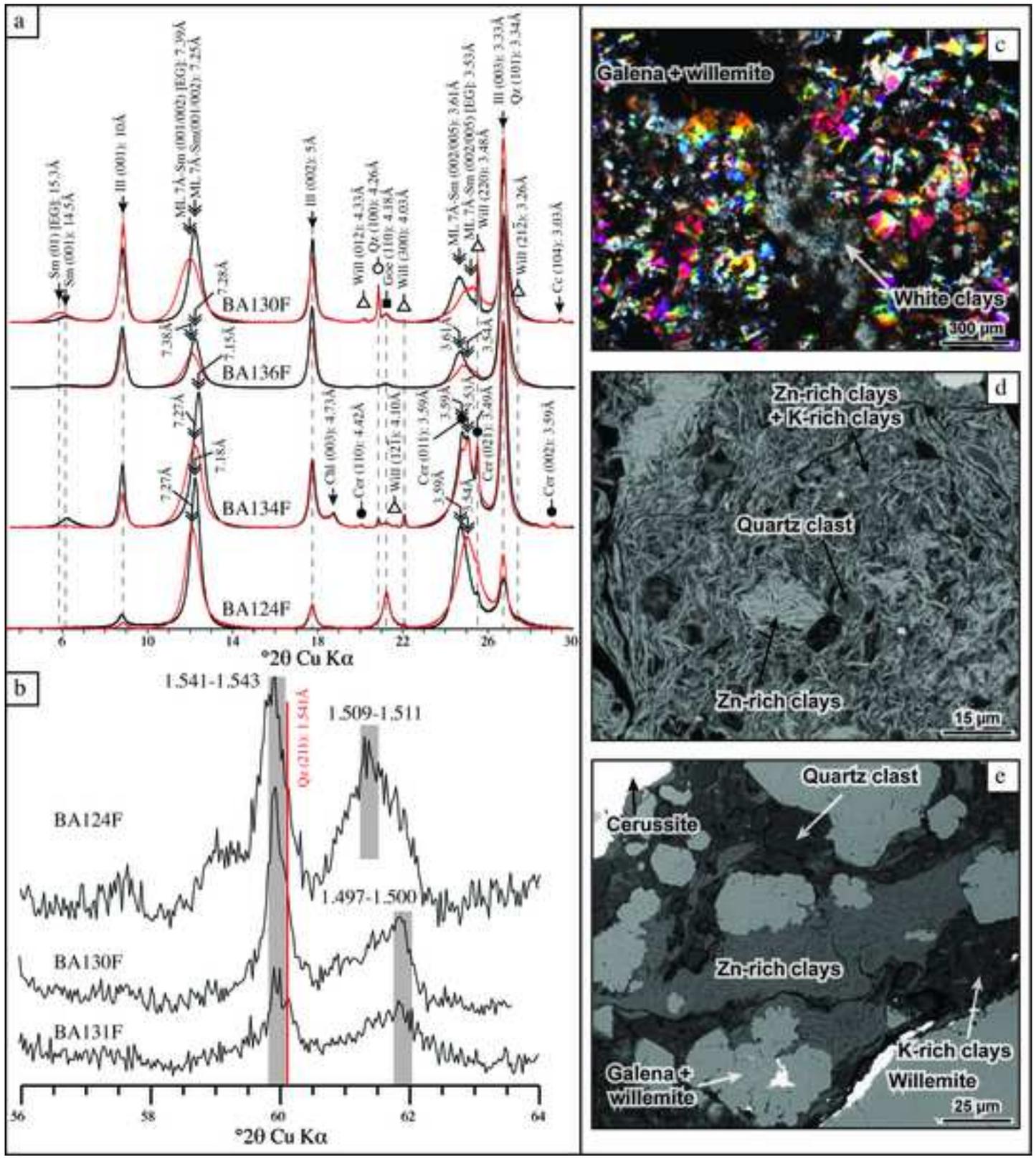
Figure 6
Click here to download Figure: Fig6.tif
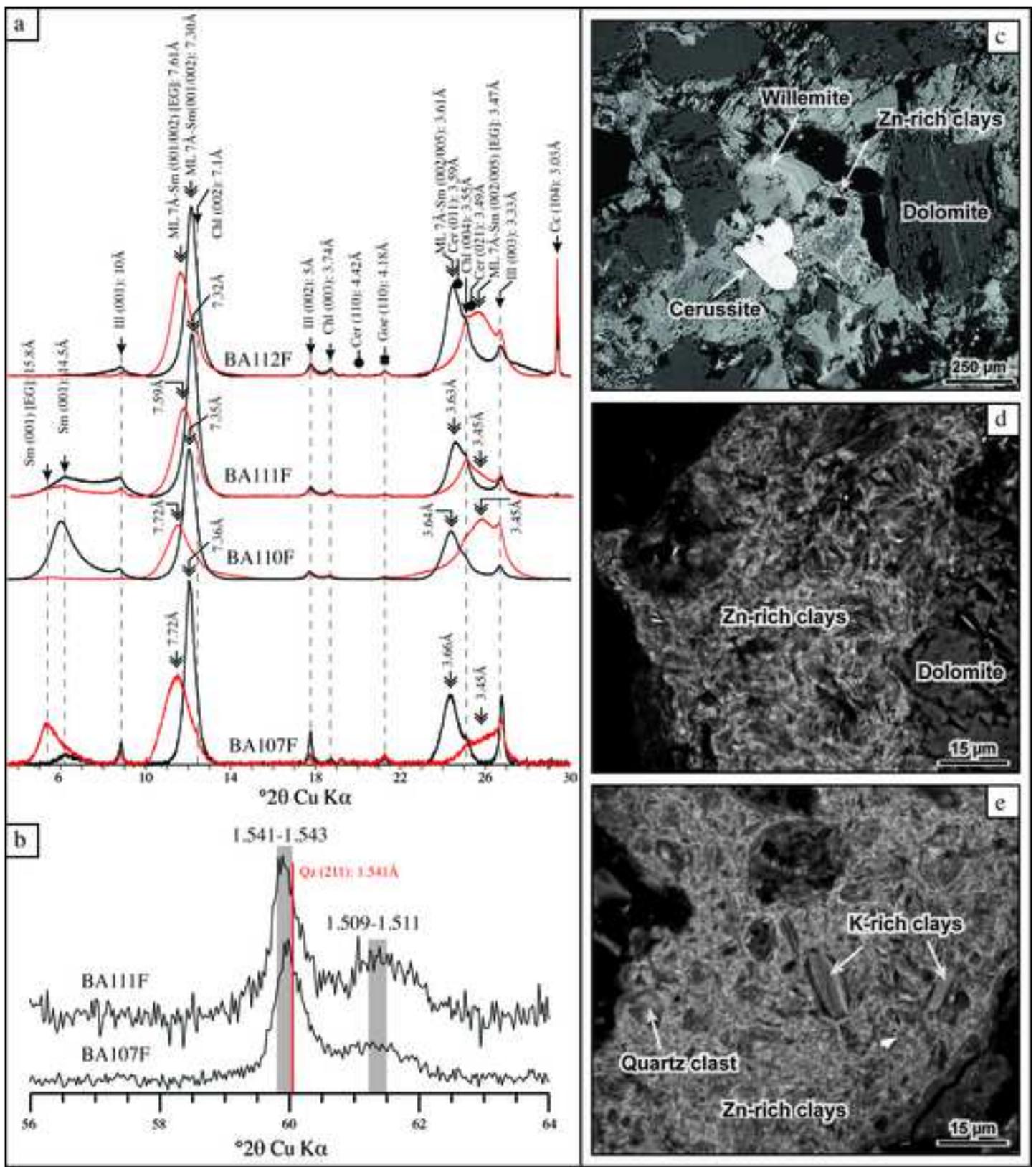
Figure 7
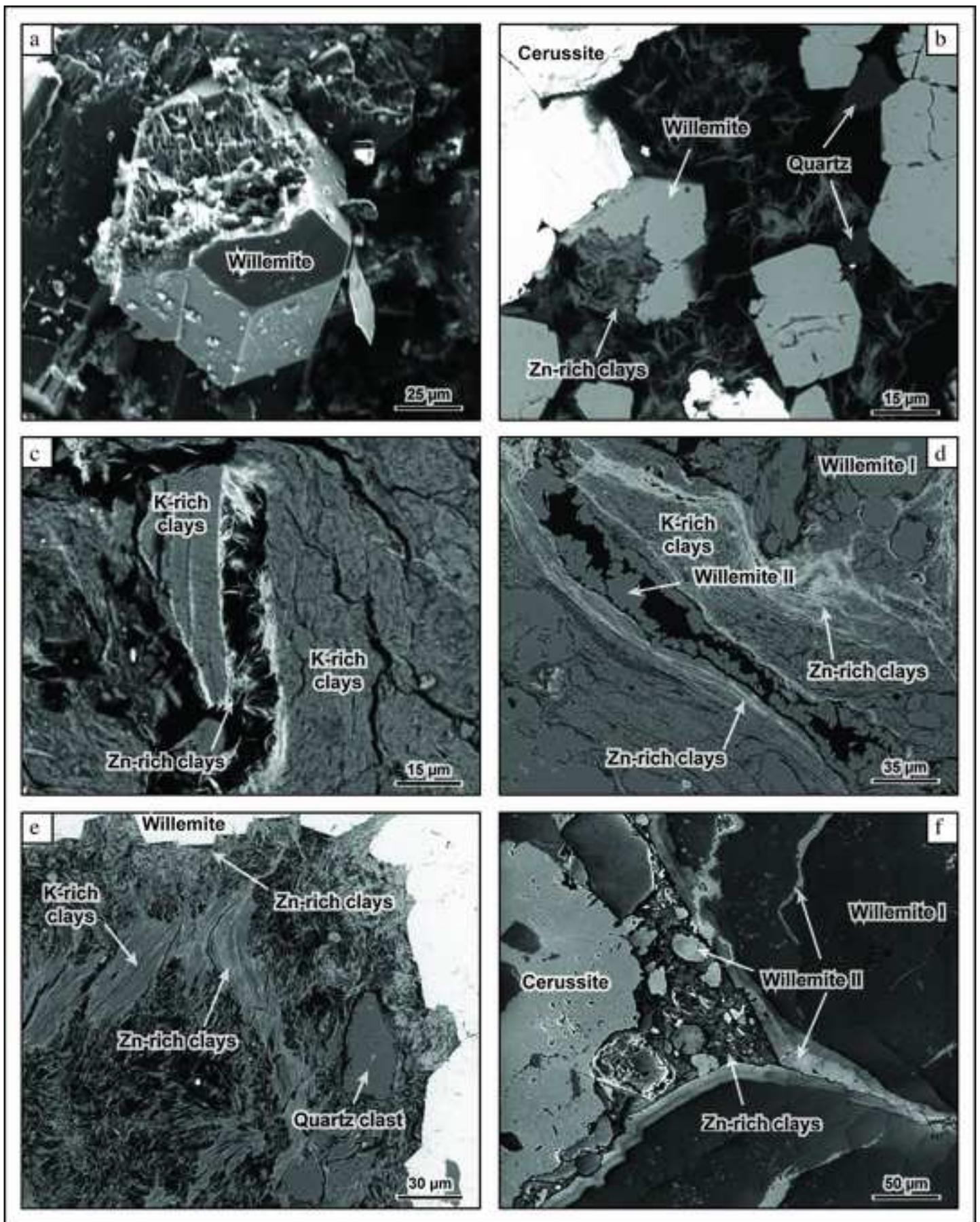
Figure 8
Click here to download Figure: Fig8.tif
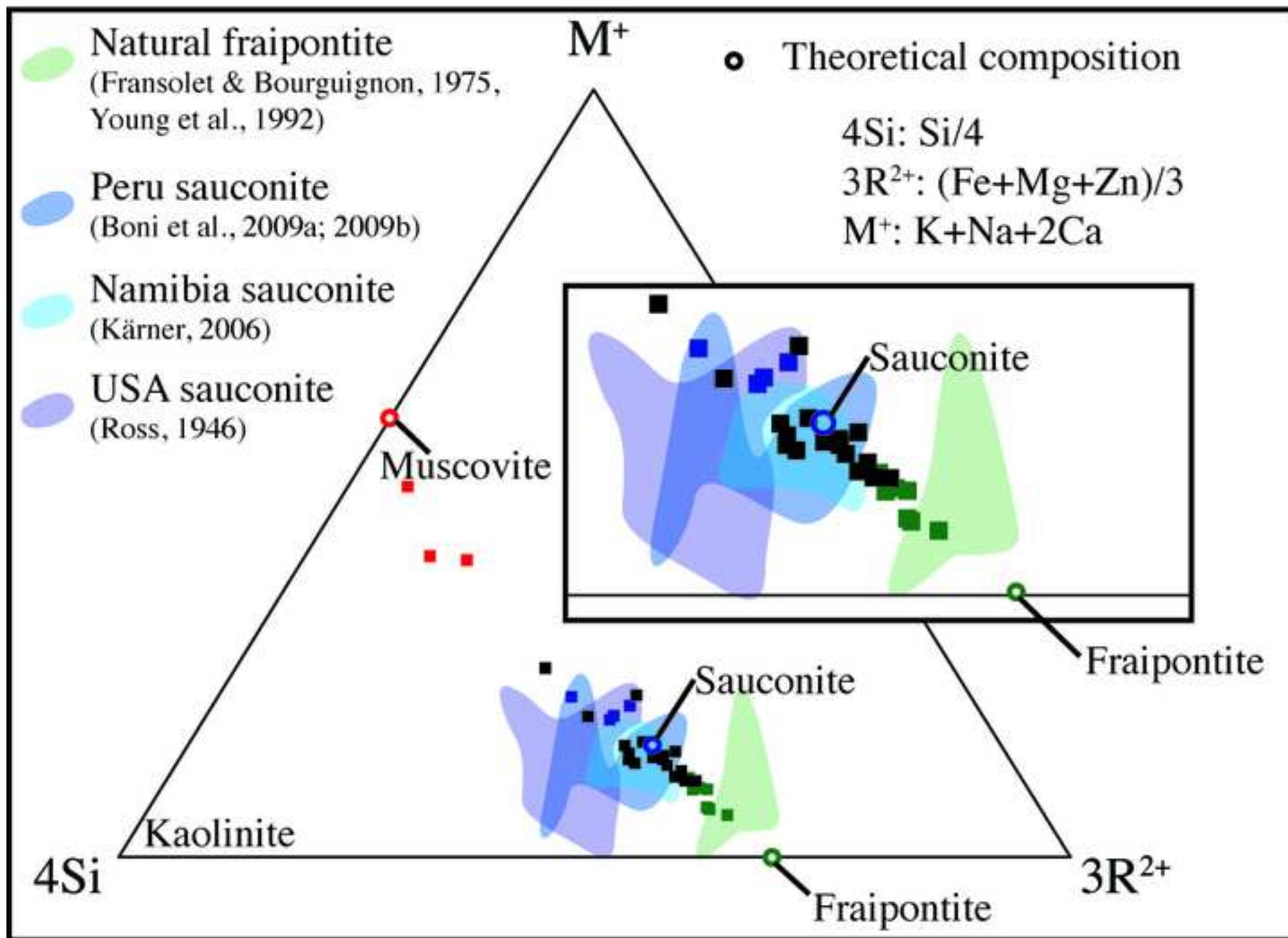
Figure 9
Click here to download Figure: Fig9.tif
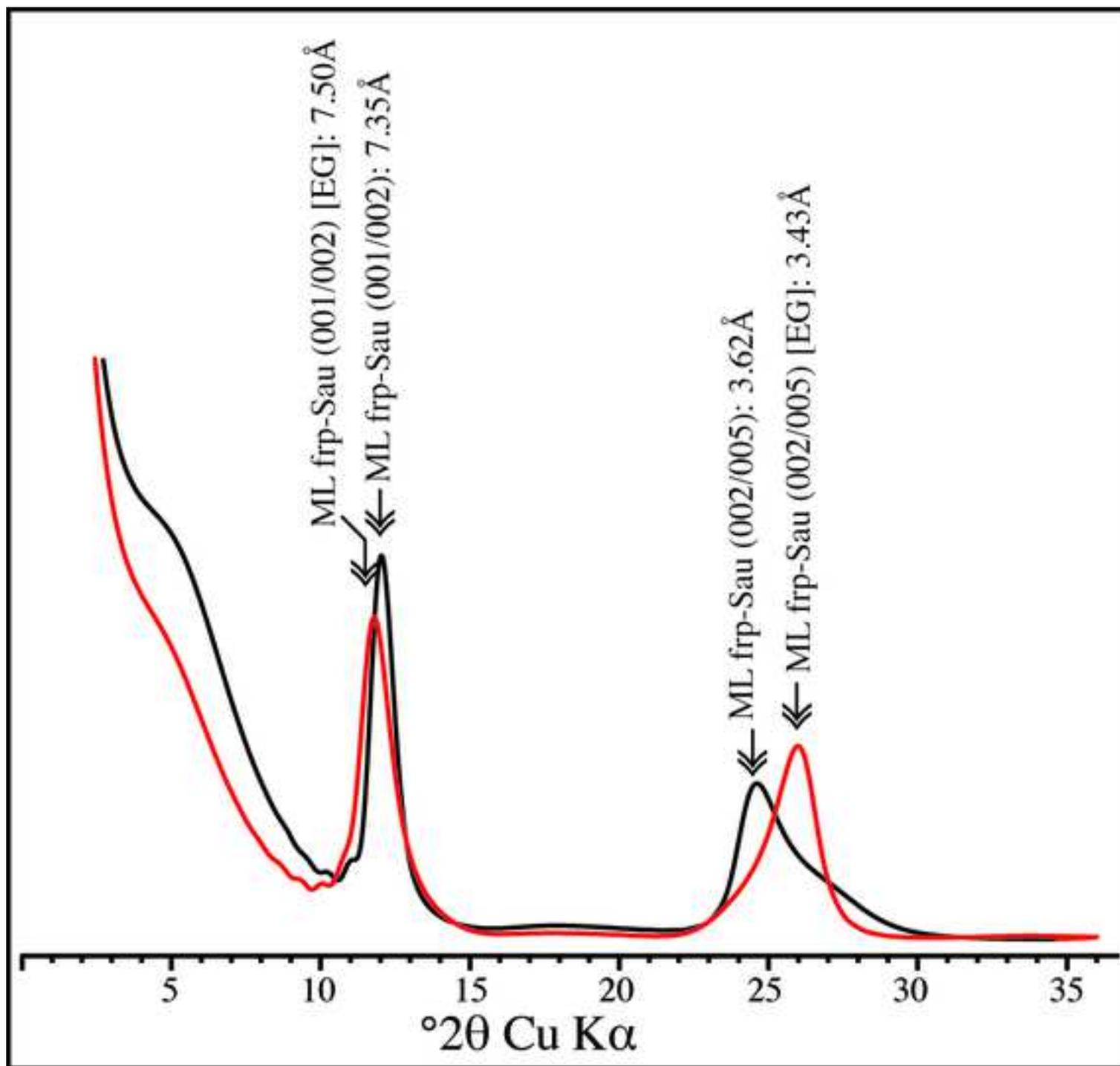
Figure 10
Click here to download Figure: Fig10.tif

Residual clays

Karstic cavities

Quartz clasts

Zn²⁺

Willemite and galena + cerussite
(secondary mineralisation + remnant of the protore)

Willemite

Detrital mica

Dolomite and calcite
(primary mineralisation)

Formation of zinc clays
- Dissolution of willemite and releasing of silica and Zn^{2+} ions
- Pervasion of zinc-rich solutions throughout the cavities filled by residual clays
- Precipitation in Si and Al- saturated domains of zinc clays growing over detrital micas of the residual clays
- Partial to total replacement of barren domains by zinc clays

Zinc clays

Table 1

Type	Sample	Mineralogy	LOI (%)	SiO2 (%)	Al2O3 (%)	Fe2O3 (%)	MgO (%)	CaO (%)	Na (%)	K2O (%)	MnO (%)	TiO2 (%)	P2O5 (%)	As (ppm)	Ba (ppm)	Cr (ppm)	Cu (ppm)	Ni (ppm)	Pb (ppm)	Sn (ppm)	Sr (ppm)	Zn (ppm)
Triassic clays																						
	BA125	qtz, cl, do, cc	20.98	31.83	8.73	4.53	8.83	19.33	0.14	0.94	0.08	0.57	0.15	119	115	49	60	50	90	160	51	1409
	BA139	qtz, cc, cl, goe	19.44	29.13	10.1	8.33	0.71	20.91	0.12	2.85	0.05	0.5	0.71	2177	71	163	293	85	27400	84	116	27600
	BA141	do, qtz, cl, cc, goe																				
	BA142	cl, qtz, goe, he, cc	6.04	45.3	14.1	24.57	1	0.81	0.1	4.38	0.06	0.73	0.31	726	136	70	166	28	9520	106	40	9672
	BA143	qtz, cl, he, do	6.1	59.98	12.15	8.12	7.58	1.07	0.0861	1.8	0.02	0.86	0.14	98	232	75	98	49	453	146	30	15000
	BA144	qtz, do, cl	13.6	45.66	11.58	6.2	11.92	6.34	0.0968	1.34	0.09	0.77	0.16	72	349	59	169	49	1020	152	34	19300
	BA149	qz, gy, cl	9.23	46.87	11.45	5.82	9.57	8.58	-	1.18	0.01	0.72	0.18	92	277	85	26	49	48	101	376	60
Jurassic rocks																						
	BA147	qtz, cc, cl, do	20.22	37.15	10.94	5.52	3.96	16.89	0.31	2.95	0.05	0.59	0.15	194	372	41	59	40	115	207	225	301
	BA148	cc, do, cl, qtz	34.68	17.19	1.94	1.92	1.04	40.88	0.0758	0.35	0.09	0.11	0.09	86	110	17	83	27	80	158	419	186
			34.8	17.18	2.06	1.93	1.08	40.43	0.0765	0.38	0.09	0.1	0.1	64	131	15	83	31	79	159	433	197
	BA148bis	cc, qtz, cl																				
	BA150	cc, cl, do, qtz	41.76	3.79	0.92	1.73	6.11	43.91	-	nd	0.18	0.09	0.04	109	100	14	43	nd	148	100	83	392
	BA151	cc, do, cl, qtz																				
	BA152	do, cc, cl, qtz																				
	BA153	do, ce, qtz, cl, do, ga	27.06	14.8	2.29	0.94	2.46	25.86	-	0.13	0.05	0.16	0.11	306	108	31	218	nd	221200	66	219	25700
	BA154	qtz, cc, cl																				
	BA156	do, cc, cl, qtz	43.86	2.37	1.17	1.32	13.13	36.6	-	0.21	0.1	0.08	0.06	118	10	16	23	nd	941	80	145	2588
	BA157	cc, qtz, cl	25.15	29.56	7.82	3.07	h	27.7	-	1.98	0.04	0.5	0.12	159	105	39	98	40	157	147	299	214
	BA158	do, cc, cl	44.94	0.51	0.3	1.95	11.94	37.94	-	nd	0.14	0.02	0.07	109	70	11	52	nd	145	153	53	381
	BA159	do, cc, qtz, cl	37.13	10.01	4.97	2.19	6.71	35.78	-	1.1	0.34	0.29	0.14	34	424	29	37	54	919	142	83	403
	BA160	cc, qtz, cl, goe	26.41	30.36	5.27	6.5	0.44	28	-	1.01	0.09	0.4	0.16	141	79	38	97	nd	1400	111	118	919
			26.43	30.25	5.34	6.69	0.44	27.9	-	0.98	0.09	0.42	0.17	181	83	39	103	38	1349	115	120	937
Red clays																						
	BA101	qtz, cc, cl	15.25	50.62	6.31	3.43	0.33	16.54	0.15	0.57	0.06	0.85	0.17	82	93	61	261	214	526	120	91	830
	BA113	qtz, cl, do	3.89	77.06	7.78	5.57	0.83	0.97	0.11	0.84	0.1	0.8	0.1	83	126	61	114	72	753	142	40	3495
	BA115	qtz, cl	7.9	50.68	20.49	8.87	1.79	0.64	0.16	2.53	0.06	1.17	0.15	469	361	112	173	65	1657	46	110	8495
	BA116	qtz, cl, cc																				
	BA121	qtz, cl, goe	7.62	52.99	18.99	10.02	1.75	0.5	0.11	2.35	0.03	1.15	0.2	327	228	89	159	36	1732	51	96	30000
	BA126	qtz, cc, cl	7.15	73.49	3.38	1.79	0.17	7.95	0.1	0.31	0.05	0.45	0.1	274	488	40	98	42	1869	142	37	9352
	BA127	qtz, cc, cl	8.76	49.62	18.42	7.19	2.17	2.07	0.12	1.87	0.02	1.04	0.13	149	308	86	179	84	1214	88	115	47300
	BA132	qtz, cl, cc																				
	BA137	qtz, cl, cc, ce	8.21	62.24	14.48	6.1	1.44	3.57	0.0881	1.76	0.03	0.98	0.1	101	195	78	109	43	1097	140	76	6362
White Clays																						
	BA117	will, ce, cc, cl, qtz, do, ga																				
	BA118	ce, will, cl, qtz, cc, ga, do																				
	BA124	will, cl, ce, goe, qtz, cc	15.66	18.21	1.78	3.24	LD	20.89	0.0778	0.25	0.03	0.1	0.33	459	49	43	193	56	8094	210	47	322400
	BA128	will, cl, ce, ga																				
	BA130	qtz, will, cl, cc, do	9.13	47.32	5.36	2.08	0.92	8.32	0.21	1.17	0.02	0.34	0.24	1133	176	138	255	34	9218	101	53	180900
	BA131	qtz, cc, cl, will, do																				
	BA133	will, qtz, cl, do, cc																				
	BA134	will, ce, qtz, cl, ga																				
	BA135	will, cl, cc, qtz, ce, ga, goe																				
	BA136	qtz, cl, do, will, ce	25.86	29.94	6.95	1.43	10.36	16.97	0.0926	1.88	0.16	0.36	0.17	411	46	69	127	36	37100	138	237	17400
	BA138	will, cl,ce, qtz, ga																				
	BA145	do, ce, cl, qtz, ga																				
Ocher clays																						
	BA102	qtz, do, cl, dol	9.65	47.09	17.89	10.41	3.41	4.01	0.18	2.32	0.12	1.13	0.09	574	451	140	10848	117	3202	137	73	7748
	BA103	do, cc, cl, qtz																				
	BA104	cc, cl, do, qtz	15.57	31.13	14.94	7.99	2.96	11.46	0.18	1.87	0.18	1.14	0.11	586	8530	85	223	125	3321	182	161	64600
	BA107	cl, cc, do, qtz	14.02	26.12	9.6	7.93	2.66	7.58	0.14	0.85	0.12	0.71	0.11	389	84	58	401	180	1384	131	70	237000
	BA108	qtz, cc, cl, do	17.56	32.67	7.56	15.2	3.75	15.86	0.15	1.23	0.1	0.44	0.19	590	240	103	488	73	4273	72	68	27600
	BA110	do, cl, qtz, cc, ce	26.66	16.49	5.45	2.29	1.8	29.3	0.2	0.5	0.07	0.31	0.09	146	49	41	564	154	27100	149	135	92000
	BA111	cl, do, cc, qtz																				
	BA112	cc, cl, do, qtz																				
	BA114	qtz, cl, do, cc	7.64	59.21	18.52	4.69	1.36	0.68	0.16	1.75	0.04	1.38	0.13	88	237	114	135	66	949	57	111	21500
	BA119	cc, cl, ce, qtz, do	39.26	5.45	2.67	1	0.76	43.52	0.13	0.66	0.05	0.16	0.1	271	31	32	73	36	19440	51	315	6275
	BA123	qtz, cl, cc, do	8.59	53.29	20.17	7.88	1.95	1.73	0.14	2.21	0.08	1.1	0.14	195	263	100	100	48	2394	70	102	18400
	BA146	qtz, do, cl, cc	20	37.98	12.29	2.11	7.45	11.31	0.11	3.13	0.05	0.69	0.16	137	269	54	40	26	1598	161	58	7408

Table 2

Type	Clay content	Sample	CEC (meq/100g)	[Zn] (%) of the CEC
Red Clays	kaol > ill >> chl	BA121	34	40.873
	kaol >> ill (ML ill/sm) > chl	BA127	30	0.235
	kaol > ill (IS ill/sm) >> chl	BA132	35	0.167
	kaol > ill (IS ill/sm) >> chl	BA137	38	0.047
White Clays	White Clays			
	ML (7Å/sm) >> ill	BA124	13	1.555
	ill > ML (7Å/sm) >> sm	BA130	12	0.168
	ML (7Å/sm) > ill >> chl > sm (not presented)	BA131	27	0.121
	ill > ML (7Å/sm)	BA136	9	0.486
Ocher Clays	Ocher Clays			
	ML (7Å/sm) > sm >> ill	BA107	41	0.055
	ML (7Å/sm) > ill >> sm (not presented)	BA108	19	0.000
	ML (7Å/sm) > sm >> ill > chl	BA110	40	0.046
	ML (7Å/sm) >> sm > ill > chl	BA111	34	0.594

Table 3

	58	57	10		19	29	20	38		26	37	55	53	49	27	43
Al₂O₃	30,418	27,047	28,727		14,142	13,862	13,504	14,166		10,929	10,727	11,835	12,150	10,962	11,582	12,421
SiO₂	48,994	44,774	42,446		34,286	31,786	32,332	30,827		29,163	30,267	28,472	30,337	27,784	30,093	29,862
MgO	1,661	1,659	0,696		1,220	0,909	1,455	1,042		0,598	0,783	0,732	0,719	0,617	0,571	0,639
FeO	1,365	1,212	1,791		3,022	3,821	2,092	3,045		1,733	2,496	0,841	0,935	0,921	1,443	0,890
CaO	0,136	0,169	0,304		0,669	0,550	0,778	1,053		0,789	0,830	0,535	0,506	0,451	0,646	0,472
K₂O	10,005	7,477	6,333		2,286	1,954	1,756	1,526		0,220	0,400	0,612	0,668	0,172	0,054	0,290
ZnO	1,860	12,984	8,316		24,677	28,583	31,004	31,929		45,455	43,963	46,668	46,254	49,392	48,535	48,882
PbO	0,180	0,196	0,379		0,395	0,284	0,205	0,306		0,197	0,146	0,103	0,161	0,256	0,037	0,183
Total	94,776	95,877	89,203		81,900	82,765	84,424	85,379		91,056	91,594	92,058	93,831	92,709	95,044	95,999
	Micas (calculated on 11O)				Sauconite (calculated on 11O)					Fraipontite (calculated on 14O)						
Si	3,300	3,168	3,137		3,185	3,024	3,031	2,909		3,563	3,641	3,463	3,564	3,419	3,532	3,478
Al(T)	0,700	0,832	0,863		0,815	0,976	0,969	1,091		0,437	0,359	0,537	0,436	0,581	0,468	0,522
Al(O)	1,714	1,425	1,640		0,733	0,578	0,523	0,485		1,137	1,162	1,160	1,247	1,009	1,134	1,183
Mg	0,167	0,175	0,077		0,169	0,129	0,203	0,147		0,109	0,140	0,133	0,126	0,113	0,100	0,111
Fe	0,077	0,072	0,111		0,235	0,304	0,164	0,240		0,177	0,251	0,086	0,092	0,095	0,142	0,087
Zn	0,092	0,678	0,454		1,692	2,007	2,145	2,225		4,100	3,904	4,190	4,011	4,487	4,205	4,203
Ca	0,010	0,013	0,024		0,067	0,056	0,078	0,106		0,103	0,107	0,070	0,064	0,060	0,081	0,059
K	0,860	0,675	0,597		0,271	0,237	0,210	0,184		0,034	0,061	0,095	0,100	0,027	0,008	0,043
Pb	0,003	0,004	0,007		0,009	0,007	0,005	0,007		0,006	0,005	0,003	0,005	0,008	0,001	0,005
ΣT	4,000	4,000	4,000		4,000	4,000	4,000	4,000		4,000	4,000	4,000	4,000	4,000	4,000	4,000
ΣOc	2,053	2,353	2,289		2,839	3,025	3,040	3,104		5,529	5,461	5,571	5,481	5,713	5,582	5,589
ΣI	0,869	0,688	0,621		0,337	0,293	0,288	0,290		0,137	0,168	0,165	0,164	0,087	0,089	0,102
ΣCh(T)	-0,700	-0,832	-0,863		-0,815	-0,976	-0,969	-1,091		-0,437	-0,359	-0,537	-0,436	-0,581	-0,468	-0,522
ΣCh(O)	-0,179	0,131	0,217		0,411	0,627	0,603	0,694		0,196	0,084	0,303	0,208	0,435	0,298	0,361
ΣCh(I)	0,879	0,701	0,645		0,404	0,349	0,366	0,397		0,241	0,275	0,234	0,228	0,146	0,170	0,161

	31	21	15	40	30	14	8	3	50	22	48	56	9	52	45	44	61
Al₂O₃	11,268	11,430	8,227	9,586	11,714	12,228	11,835	11,218	12,275	14,723	20,423	15,514	13,779	12,885	13,088	15,033	16,004
SiO₂	27,531	31,670	31,210	28,536	29,332	33,317	32,249	34,047	28,108	36,985	38,990	32,539	36,505	31,157	32,005	32,027	32,546
MgO	0,732	1,262	0,897	0,837	1,248	0,845	0,968	0,860	0,674	1,157	2,133	0,807	1,127	0,696	0,714	0,860	0,793
FeO	6,419	2,775	1,111	1,716	3,346	2,121	2,030	1,719	0,725	2,950	3,805	0,679	2,098	1,002	1,974	1,153	0,955
CaO	0,579	0,799	1,023	0,762	0,596	0,719	0,855	0,842	0,408	0,820	0,293	1,039	0,868	0,485	0,479	0,340	0,301
K₂O	1,185	0,799	0,419	0,271	1,105	0,901	1,114	0,657	0,938	1,833	3,874	2,103	1,198	1,106	0,995	1,528	1,726
ZnO	32,400	32,257	38,827	40,653	35,375	35,813	37,081	38,073	43,892	30,573	21,132	39,054	38,257	45,090	43,658	42,782	43,150
PbO	0,685	0,000	0,316	0,000	0,117	0,242	0,115	0,051	0,195	0,168	0,460	0,081	0,195	0,183	0,330	0,183	0,029
Total	82,403	82,421	83,625	84,317	84,510	86,185	86,247	87,468	88,989	90,477	91,870	93,782	94,025	94,729	95,262	95,744	97,420
	Mixture of mica, sauconite and/ or fraipontite (calculated on 11O)																
Si	2,833	3,085	3,140	2,915	2,893	3,076	3,017	3,119	2,736	3,157	3,087	2,850	3,070	2,820	2,799	2,855	2,783
Al(T)	1,167	0,915	0,860	1,085	1,107	0,924	0,983	0,881	1,264	0,843	0,913	1,150	0,930	1,180	1,201	1,145	1,217
Al(O)	0,199	0,397	0,116	0,069	0,255	0,407	0,322	0,330	0,144	0,639	0,992	0,452	0,436	0,195	0,348	0,231	0,396
Mg	0,112	0,183	0,135	0,127	0,183	0,116	0,135	0,117	0,098	0,147	0,252	0,105	0,141	0,094	0,112	0,095	0,101
Fe	0,552	0,226	0,093	0,147	0,276	0,164	0,159	0,132	0,059	0,211	0,252	0,050	0,148	0,076	0,084	0,147	0,068
Zn	2,461	2,319	2,883	3,065	2,576	2,441	2,560	2,574	3,154	1,927	1,235	2,525	2,375	3,013	2,760	2,874	2,723
Ca	0,064	0,083	0,110	0,083	0,063	0,071	0,086	0,083	0,043	0,075	0,025	0,097	0,078	0,047	0,032	0,046	0,028
K	0,155	0,099	0,054	0,035	0,139	0,106	0,133	0,077	0,116	0,200	0,391	0,235	0,128	0,128	0,170	0,113	0,188
Pb	0,018	0,000	0,008	0,000	0,003	0,006	0,003	0,001	0,005	0,004	0,009	0,002	0,004	0,004	0,004	0,008	0,001
ΣT	4,000	4,000	4,000	4,000	4,000	4,000	4,000	4,000	4,000	4,000	4,000	4,000	4,000	4,000	4,000	4,000	4,000
ΣOc	3,343	3,126	3,235	3,407	3,293	3,134	3,179	3,155	3,459	2,927	2,740	3,134	3,104	3,382	3,309	3,355	3,289
ΣI	0,219	0,183	0,164	0,119	0,202	0,177	0,219	0,159	0,159	0,275	0,416	0,332	0,207	0,175	0,202	0,159	0,216
ΣCh(T)	-1,167	-0,915	-0,860	-1,085	-1,107	-0,924	-0,983	-0,881	-1,264	-0,843	-0,913	-1,150	-0,930	-1,180	-1,201	-1,145	-1,217
ΣCh(O)	0,884	0,649	0,586	0,883	0,842	0,675	0,679	0,639	1,063	0,493	0,472	0,720	0,645	0,958	0,964	0,941	0,974
ΣCh(I)	0,283	0,266	0,274	0,202	0,265	0,248	0,304	0,242	0,202	0,350	0,441	0,430	0,285	0,222	0,234	0,205	0,243